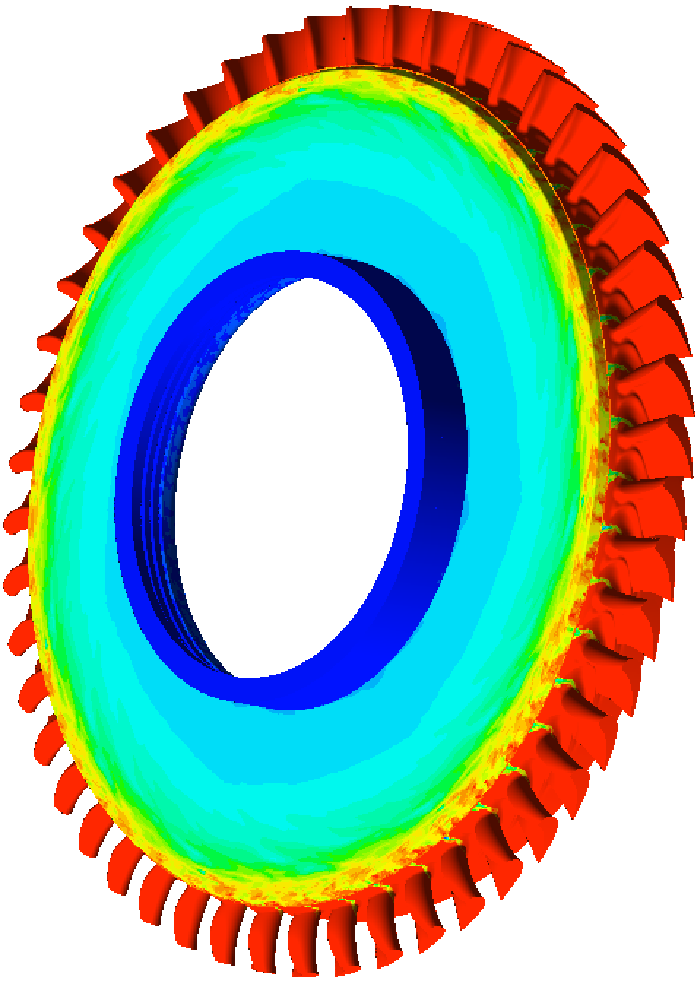

Investigation of Disc Cavity Sealing Efficiency Using CFD

Master's thesis in Applied Mechanics

YOGESH PERUVEMBA KRISHNAN

DEPARTMENT OF MECHANICS AND MARITIME SCIENCES
CHALMERS UNIVERSITY OF TECHNOLOGY
Gothenburg, Sweden 2025
www.chalmers.se

MASTER'S THESIS IN APPLIED MECHANICS

Investigation of Disc Cavity Sealing Efficiency Using CFD

YOGESH PERUVEMBA KRISHNAN

Department of Mechanics and Maritime Sciences
Division of Division Name
CHALMERS UNIVERSITY OF TECHNOLOGY
Gothenburg, Sweden 2025

Investigation of Disc Cavity Sealing Efficiency Using CFD
YOGESH PERUVEMBA KRISHNAN

Supervisor: Navid Mikaillian, Siemens Energy AB.
Examiner: Tomas Grönstedt, Department of Mechanics and Maritime Sciences.

Master's Thesis 2025
Department of Mechanics and Maritime Sciences
Division of Fluid Dynamics
Chalmers University of Technology
SE-412 96 Gothenburg
Sweden
Telephone +46 31 772 1000

Cover: Instantaneous hot gas mass fraction for DR =1, $\Phi_0 = 0.025$ using SBES turbulence model (duplicated to 360°).

Typeset in LaTeX
Gothenburg, Sweden 2025

Investigation of Disc Cavity Sealing Efficiency Using CFD
YOGESH PERUVEMBA KRISHNAN

Department of Mechanics and Maritime Sciences
Division of Fluid Dynamics
Chalmers University of Technology

Abstract

The wheelspace cavity between a stator and rotor disc in gas turbines are prone to ingestion of hot gases which threatens the lifetime and safe operation of the turbine. Traditionally, pressurized cooling gas known as, *Purge gas*, is bled from compressor stage to seal the cavity. The influence of purge - mainstream density ratio (DR), plays a vital role in efficient sealing of the cavity and holds significant practical implications for future engine designers.

Building upon prior experimental tests performed at KTH University in collaboration with Siemens Energy AB, the thesis primarily investigates the influence of this DR using CFD simulations. The investigation is carried out at design point of 10540 RPM ($C_f = 0.35$) for three purge flow rates 0.5%, 1.0%, 1.5% ($\Phi_0 = 0.025, 0.050,\ 0.075$) of main annulus mass flow. The tested purge gases are Air (DR =1) and Argon (DR = 1.38). The simulations are performed in Ansys CFX with increasing modeling complexity starting from steady state RANS to URANS and hybrid RANS- LES model, SBES. Further, a comparison of computational domains, single passage and 51° sector domain was also evaluated.

The results highlight the importance of sector domain over single passage domain and the need for URANS simulations to capture the unsteady ingress phenomenon. The ingress is evaluated using the non-dimensional variable, *Sealing Effectiveness*, at various radial locations. Regardless of the purge gas, an improved sealing is observed for increasing purge flow rates and for decreasing radius, as expected. Validation of CFD predictions showed a good agreement for Air (DR =1). While for Argon (DR = 1.38), an increased sealing is predicted directly contradicting experimental conclusion. This discrepancy was attributed to the seed gas concentration level (1% CO_2) used in the experiment resulting in overestimation of ingress.

For the low purge flow rate $\Phi_0 = 0.025$, regardless of purge gas a poor agreement was observed owing to the slow convection rate. While a longer simulation run performed using SBES showed relative improvement, the case still warrants further investigation.

Keywords : Gas turbines, Wheelspace cavity, Cavity purge flow, Ingress, CFD, Density ratio, Sealing effectiveness.

Preface

This report presents the outcome of master's thesis project carried out at Siemens Energy AB, Sweden, in collaboration with KTH University, during the spring of 2025. The project is supervised by Navid Mikaillian of Siemens Energy and examined by Tomas Grönstedt of Chalmers University of Technology.

Acknowledgements

First and foremost, I wish to express my sincerest gratitude to my supervisor, Navid Mikaillian of Siemens Energy AB. His mentorship and support were invaluable in navigating the hurdles faced throughout this thesis. I would like to extend my gratitude to Nils Rignell of Siemens Energy AB for his insights on the topic and for reviewing my report.

Secondly, I am grateful to Jens Fridh of KTH University for his guidance and feedback. I thoroughly enjoyed the engaging and insightful discussions during the meetings which contributed greatly to this work.

My gratitude to Chalmers University and my examiner Tomas Grönstedt for taking the time to evaluate my thesis and providing feedback and ultimately making this work better.

A big thank you also goes out to my fellow thesis students for all the fika sessions and the friendly banters.

Finally, my heartfelt thanks go out to my family and friends for their immense support throughout this journey. Their encouragement made me to believe in myself and kept me strong through all the challenges faced.

Yogesh Peruvemba Krishnan, Gothenburg, August 2025

I am batman

List of Acronyms

Below is the list of acronyms that have been used throughout this thesis listed in alphabetical order:

CFD	Computational Fluid Dynamics
CFL	Courant-Freidrichs Lewy Number
CI	Combined Ingress
DR	Density Ratio
EI	Externally Induced ingress
HPT	High Pressure Turbine
KTH	Kungliga Tekniska Högskolan
LES	Large Eddy Simulations
MFR	Mass Flow Ratio
RANS	Reynolds Averaged Navier Stokes
RI	Rotationally Induced ingress
SAS	Secondary Air Systems
SBES	Stress Blended Eddy Simulation
SDES	Shielded Detached Eddy Simulation
SE	Siemens Energy AB
SP	Single Passage
SRS	Scale Resolving Simulations
SST	Shear Stress Transport
TET	Turbine Entrance Temperature
URANS	Unsteady Reynolds Averaged Navier Stokes
WALE	Wall Adapting Local Eddy viscosity

Nomenclature

Below is the nomenclature of indices, sets, parameters, and variables that have been used throughout this thesis.

Variables

a	Cavity axial distance
b	Hub radius
C_f	Flow coefficient
c	Absolute velocity
c_p	Specific heat at constant pressure
c_w	Non-dimensional cavity flow rate
F	Force
G	Gap ratio
G_c	Seal clearance ratio
h	Enthalpy
L_t	Turbulence length scale
m	Mass
$\dot{m}$	Mass flow
$\dot{m}_p$	Mass flow of purge gas
$(m_p)_{annulus}$	Purge gas mass fraction in annulus
$(m_p)_{local}$	Local purge gas mass fraction
$(m_p)_{purge}$	Purge gas mass fraction at purge inlet
N_b	Number of rotor blades
N_v	Number of stator vanes
P	Pressure
PR	Pitch ratio
r	Radius

Re_{c_x}	Axial Reynolds Number
Re_θ	Rotational Reynolds Number
s_c	Seal clearance ratio
T	Temperature
U	Mean flow velocity through rim seal
u	Blade speed
v	Velocity
W	Work
γ_{inlet}	Ambient seed gas concentration
γ_o	Seed gas concentration at purge inlet
γ_s	Local seed gas concentration
w	Relative velocity
y^+	Wall Y plus

Symbols

α	Absolute flow angle
β	Relative flow angle
ϵ	Sealing effectiveness
ϵ_m	Mass effectiveness
η_{ts}	Total to static efficiency
η_{tt}	Total to total efficiency
κ	Ratio of specific heats
λ	Thermal conductivity
μ	Dynamic viscosity
Ω	Angular velocity
ρ	Density
Φ	Non-dimensional sealing parameter
τ	Torque

Subscripts

0	Total condition
1	Stator inlet

2	Stator outlet / Rotor inlet
3	Rotor outlet
e	Egress
i	Ingress
m	Meridional component
o	Purge flow
r	Radial component
θ	Circumferential/Tangential component
x	Axial component

Contents

List of Acronyms **ix**

Nomenclature **xi**

List of Figures **xvii**

List of Tables **xix**

1 Introduction **1**
- 1.1 Objectives 2
- 1.2 Background of the experimental work 2
- 1.3 Delimitations 4
- 1.4 Report outline 4

2 Theory **5**
- 2.1 Fundamentals of the gas turbine engine 5
  - 2.1.1 Working principle 5
  - 2.1.2 The axial turbine 6
    - 2.1.2.1 Velocity triangles 6
    - 2.1.2.2 Euler turbine equation 7
    - 2.1.2.3 Turbine efficiency 7
    - 2.1.2.4 Secondary Air Systems (SAS) 8
- 2.2 Rotor-stator wheelspace flow 10
  - 2.2.1 Flow regimes 10
  - 2.2.2 Conceptual flow inside the wheelspace 11
  - 2.2.3 Ingress driving mechanisms 13
    - 2.2.3.1 Externally Induced (EI) ingress 13
    - 2.2.3.2 Rotationally Induced (RI) ingress 14
    - 2.2.3.3 Combined Ingress (CI) 14
    - 2.2.3.4 Rim seal instabilities 14
    - 2.2.3.5 Kelvin-Helmholtz instabilities 15
    - 2.2.3.6 Taylor-Couette flows 16
  - 2.2.4 Non-dimensional coefficients 17
- 2.3 Computational Fluid Dynamics (CFD) 18
  - 2.3.1 RANS 18
  - 2.3.2 URANS 19
  - 2.3.3 Shear Stress Transport (SST) $k-\omega$ model 20

2.3.4 Stress Blended Eddy Simulation (SBES) 21
2.3.4.1 Concept of LES 21
2.3.4.2 WALE LES 22
2.3.4.3 Shielding in SBES 22

3 Methodology **25**
3.1 Meshing process 25
3.2 Simulation setup 27
3.2.1 Computational domain 27
3.2.2 Thermodynamic properties 27
3.2.3 Boundary conditions 28
3.2.4 Solver settings 30
3.2.4.1 Steady state 30
3.2.4.2 URANS 30
3.2.4.3 SBES 31
3.3 Estimation of sealing effectiveness (ε) in CFD 31
3.4 Transient simulation - Monitor points 32

4 Results **35**
4.1 Mesh study 36
4.2 Steady state simulations - Single Passage (SP) domain 38
4.2.1 Effect of purge flow rate at constant density ratio 38
4.2.2 Effect of density ratio at constant purge flow $\Phi_0 = 0.050$ . . . 39
4.2.3 Comparison of sealing effectiveness 39
4.3 Steady state simulations - Sector domain 40
4.3.1 Evaluation of density effects - Sector domain 41
4.3.2 Comparison between SP and Sector domain 42
4.4 URANS simulations 44
4.4.1 Comparison between DR = 1 and DR = 1.38 for $\Phi_0 = 0.075$. 45
4.4.2 Comparison between DR = 1 and DR = 1.38 for $\Phi_0 = 0.050$. 47
4.4.3 Comparison between DR = 1 and DR = 1.38 for $\Phi_0 = 0.025$. 49
4.5 Effect of purge-mainstream density 51
4.6 SBES simulations 53
4.6.1 Comparison of URANS vs SBES 53
4.6.2 Time averaged results 55

5 Conclusion **59**
5.1 Recommendations for future work 60

A Appendix **I**
A.1 SBES: Mesh evaluation I
A.2 SBES: Shielding function II

List of Figures

1.1 Cross-sectional view of turbine wheelspace. Main-annulus flow in red, purge flow in blue [1]. 2
1.2 KTH test turbine [2]. 3

2.1 Schematic of a generalized gas turbine engine. 5
2.2 Velocity triangles for an axial turbine stage [3]. 6
2.3 Ideal and actual Brayton cycle. 8
2.4 Schematic of SAS in a gas turbine [4]. 9
2.5 Flow regimes inside the wheelspace. Adopted from [5]. 10
2.6 Key dimensions of wheelspace cavity. 11
2.7 Flow in wheelspace with (a) separated and (b) merged boundary layers [1]. 12
2.8 Flow in the wheelspace for (a) $\Phi_o < \Phi_{min}$ and (b) $\Phi_o = \Phi_{min}$ [6]. . . . 12
2.9 Hot gas ingress driving mechanisms [7]. 13
2.10 Disc pumping effect [5]. 14
2.11 Common rim seal configurations [5]. 15
2.12 Large scale flow structures inside cavity - 90° sector model [8]. 15
2.13 Formation of Kelvin - Helmholtz vortical structures [9]. 16
2.14 Taylor-Couette instability [10]. 16
2.15 Representation of a large and a sub grid scale eddy. 22

3.1 Illustration of 3D mesh. 26
3.2 Stage domains for CFD analysis. (a) SP domain (b) Sector domain . 27
3.3 Thermodynamic properties of Argon (DR = 1.38) as a function of temperature. 28
3.4 Domain boundary conditions. 29
3.5 Normalized radial pressure profile at the main inlet. 29
3.6 Sealing effectiveness measurement locations. 31
3.7 Location of monitor points in the domain. 33

4.1 Result analysis framework. 35
4.2 Contour plot of wall y^+ for base mesh with high y^+ region enlarged. . 36
4.3 Line probe locations 36
4.4 XY plot of total pressure profiles at different locations. 37
4.5 SP domain - contour plot of hot gas mass fraction in meridional view. 38
4.6 SP domain - contour plot of hot gas mass fraction from isometric top-down point of view. 39

4.7 SP Domain - Comparison of sealing effectiveness experiment vs steady CFD. 40
4.8 Sector domain - contour plot of hot gas mass fraction in isometric top-down point of view. 41
4.9 Sector domain - pitchwise variation of static pressure at blade rim seal for $\Phi = 0.050$. 41
4.10 Comparison of hot gas mass fraction, SP vs Sector domain for DR = 1 $\Phi_0 = 0.025$ (contour plot with 21 levels). 42
4.11 Comparison of sealing effectiveness for DR =1, $\Phi_0 = 0.025$. Experiment vs SP domain vs Sector domain. 43
4.12 Comparison of pitchwise pressure variation, SP vs Sector domain. . . 43
4.13 Isovolume of cavity with CFL ≤ 5 limiter for DR =1, $\Phi_0 = 0.075$. . . 45
4.14 Time averaged hot gas mass fraction for DR = 1. 46
4.15 Time averaged hot gas mass fraction for DR = 1.38 46
4.16 Time and circumferential averaged sealing effectiveness comparison experiment vs CFD for $\Phi_0 = 0.075$. 47
4.17 Time averaged hot gas mass fraction for DR = 1. 48
4.18 Time averaged hot gas mass fraction for DR = 1.38 48
4.19 Time and circumferential averaged sealing effectiveness comparison experiment vs CFD for $\Phi_0 = 0.050$. 49
4.20 Time averaged hot gas mass fraction for DR = 1. 50
4.21 Time averaged hot gas mass fraction for DR = 1.38 50
4.22 Time and circumferential averaged sealing effectiveness comparison experiment vs CFD for $\Phi_0 = 0.025$. 51
4.23 Time and circumferential averaged sealing effectiveness comparison experiment vs CFD consolidated. Adopted from [11]. 52
4.24 Sealing effectiveness vs Φ_o curve. Experimental and computational data. Open circles - experiment, blue - CFD with 1% purge CO_2 seeding and red - CFD with 100% purge CO_2 seeding [12]. 53
4.25 Instantaneous hot gas mass fraction with URANS at 3 revolutions. . 54
4.26 Instantaneous hot gas mass fraction with SBES at 3 revolutions. . . . 54
4.27 Circumferentially averaged sealing effectiveness comparison at a time instant. URANS vs SBES. 55
4.28 Time averaged hot gas mass fraction for DR = 1, $\Phi_o = 0.025$ using SBES. 56
4.29 Time and circumferentially sealing effectiveness comparison for DR =1 $\Phi_o = 0.025$. 56

5.1 Computational domain utilized in [12]. 61

A.1 Isovolume of cavity with a limiter of ≤ 5. I
A.2 Contour plot of shielding function at 7 revolutions. II

List of Tables

1.1 Overview of cases tested in the experiment. 10540 RPM - on design point and 14000 RPM - off design point. 3

3.1 Quality metrics for all meshes. 25
3.2 Solver settings for steady state 30
3.3 Solver settings for URANS 31
3.4 Solver settings for SBES. 31

4.1 Non-dimensional operating parameters. 35
4.2 Steady state simulation cases. 38
4.3 URANS simulation cases. 44

1

Introduction

Industrial gas turbines play an integral role in producing clean, reliable and efficient means of energy. Unlike aircraft engines, industrial gas turbines may operate continuously at base load for longer periods. With numerous advantages over other forms of energy production, they are used in several sectors such as electrical power plants, mining industry and oil & gas refineries. Regardless of application, the essential parts are the compressor, the combustion chamber and the turbine. Over the years, the predominant focus of research was optimizing primary flows to achieve higher efficiency which led to an increase in Turbine Entrance Temperature (TET). Modern gas turbines operate in the range of 1700°C which exceeds the melting temperature of even nickel based super-alloys [1, 13]. This increased the demand on internal cooling systems to protect the blades and other areas of the turbine prone to thermal stresses.

One such area is the wheelspace cavity between a stator and rotor disc. Sufficient wheelspace clearance is required to allow for rotor movement and account for manufacturing tolerances and thermal expansion of material. Hence, active cooling is necessary to prevent unprecedented ingestion of high temperature mainstream flow as it threatens the lifetime and safety of the turbine. This is achieved by *Purge cooling*, where pressurized air is bled from a suitable compressor stage to seal the cavity. While this purge flow facilitates cooling, it ultimately mixes with the mainstream through the rim seal as shown in Figure 1.2. A superfluous amount of purge is detrimental to performance while insufficient amounts fail to seal the cavity. Therefore, an understanding of interplay between mainstream and purge flows are important. Significant research efforts were devoted to understand this interplay, including development of theoretical models, experimental tests and computational studies conducted by many institutions. While it resulted in an improved understanding of cavity aerodynamics and various ingestion governing mechanisms, many questions still remain unanswered.

One of the question is the influence of purge - mainstream density ratio (DR). Since most of the experimental studies are conducted at room temperature, they do not take this DR into account. However, recent research has shown that it has the potential to create a significant impact.

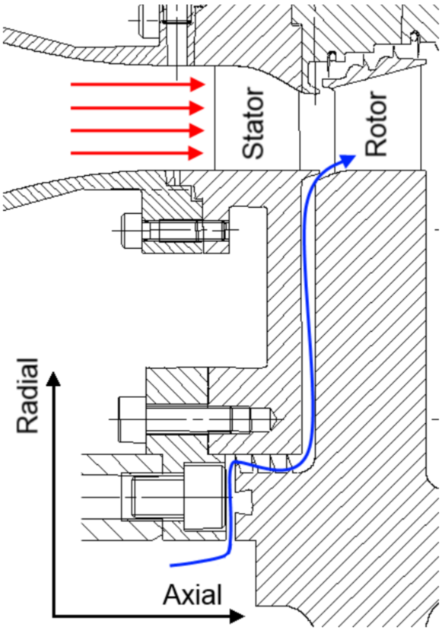

Figure 1.1: Cross-sectional view of turbine wheelspace. Main-annulus flow in red, purge flow in blue [1].

1.1 Objectives

This thesis aims to investigate the influence of purge - mainstream DR through CFD simulations. The thesis is an extension to the previous experimental work [11], conducted at KTH University in collaboration with Siemens Energy (SE). In line with this aim, the objectives are as follows :

- Perform 3D steady and transient CFD simulations under same operating conditions as experiment.
- Validate the CFD predictions against experimental estimation using non-dimensional variable, sealing effectiveness.
- Evaluate the influence of DR on hot gas ingestion.

1.2 Background of the experimental work

The test turbine facility at KTH University, is a joint venture between KTH and SE with several research focus areas as follows:

- Turbine stage performance characterization
- Efficiency measurements and interstage flow parameter investigation
- Partial admission flow investigation
- Aeromechanical investigation
- Purge flow characterization in a High Pressure Turbine (HPT) stage.

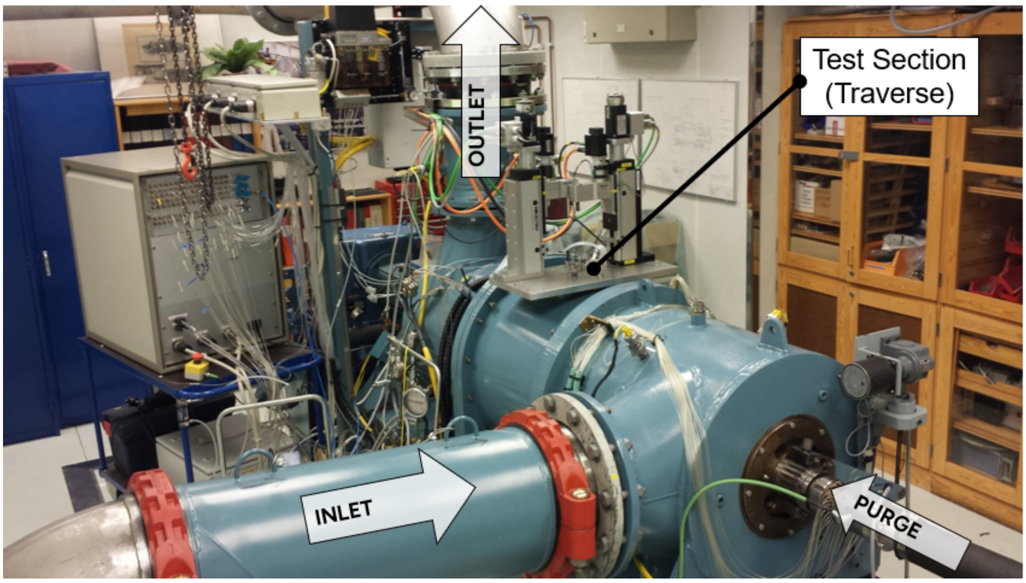

Figure 1.2: KTH test turbine [2].

Prior experiments were carried out on the HPT stage and studied the influence of DR on cavity sealing and turbine performance [11]. The tests involved two purge gases: Air (DR = 1) and Argon (DR = 1.38) which were tested at varied operating points and purge flow rates. The Table 1.1 provides an overview of the various cases tested in terms of purge - mainstream mass flow ratio (MFR). The MFR is defined as ratio of purge mass flow to the stage outlet mass flow. Also tabulated are the corresponding non-dimensional values. These non-dimensional values are defined later in Section 2.2.4.

RPM	MFR		
10540	0.5%	1.0%	1.5%
14000	0.5%	1.0%	1.5%

(a) RPM and MFR

C_f	Φ_0		
0.35	0.025	0.050	0.075
0.26	0.019	0.037	0.056

(b) Non-dimensional reference.

Table 1.1: Overview of cases tested in the experiment. 10540 RPM - on design point and 14000 RPM - off design point.

About 1% of purge mass flow was seeded with a non-reacting gas, CO_2. Ingress is evaluated using concentration based sealing effectiveness (see Equation 2.24) at various radial locations. A higher sealing effectiveness implies lower hot gas ingestion. The results revealed the following findings:

- For the same purge mass flow, the heavier purge gas (DR = 1.38) resulted in lower sealing than the lighter purge (DR = 1) and in-turn reduced stage efficiency.
- For the same purge gas, a higher RPM resulted in higher sealing effectiveness.
- With increasing purge mass flow, the efficiency reduced.

Other results include absence of compressibility effects in the cavity and evaluation of optimal fitting parameters for the orifice model [14].

1.3 Delimitations

Within the scope of this thesis, the following limitations are identified and listed below.

- The simulations are carried out only for the on-design point of 10540 RPM. The off-design cases with 14000 RPM are not simulated due to time limitations.
- Effects of heat transfer due to ingestion and structural impact are outside the scope of this study.
- The interest was limited to the cavity. Therefore, influence of purge flow in the main annulus was not considered.

1.4 Report outline

Chapter 1 introduces the topic and provides a summary of the prior experimental work carried out. In addition, objectives and limitations are listed out.

Chapter 2 briefly explains the relevant theory and literature related to basics of axial turbine, flow system in a wheelspace cavity and CFD.

Chapter 3 describes the CFD methodology including mesh generation, numerical setup and the estimation of sealing effectiveness.

Chapter 4 presents the results and validates them. In addition, discussion related to density effects are also presented.

Chapter 5 summarizes the findings of this thesis and provides recommendation for future work.

2

Theory

This chapter elucidates the theoretical concepts foundational to the thesis into three sections. The first section deals with basics of gas turbines. The second section focuses on flow in a rotor - stator wheelspace and the various ingress driving mechanisms. The final section is dedicated to CFD, discussing the turbulence models employed.

2.1 Fundamentals of the gas turbine engine

2.1.1 Working principle

The generation of power within a gas turbine engine involves a series of thermodynamic processes, fundamentally described by the Brayton cycle. The key processes in an ideal cycle are explained below with the help of Figure 2.1.

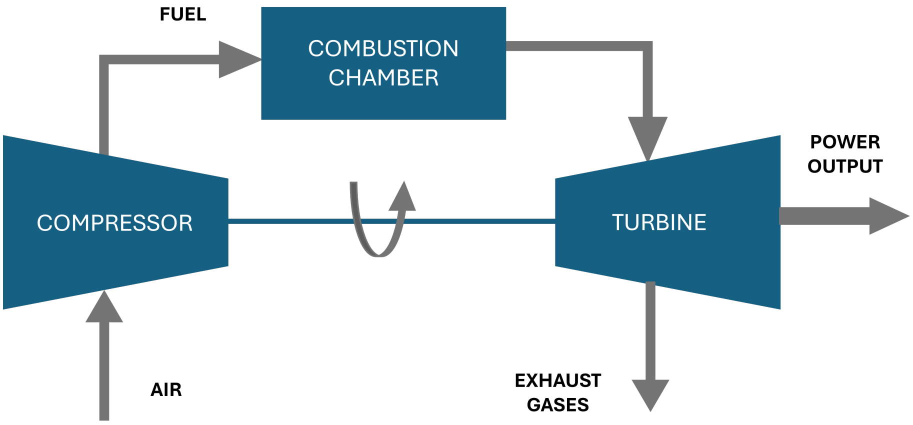

Figure 2.1: Schematic of a generalized gas turbine engine.

- The air is drawn into compressor where it is isentropically compressed resulting in increase of pressure and temperature.
- In the combustion chamber, heat is added to the compressed air under constant pressure generating high temperature gas.
- Finally in the turbine, the gas is allowed to expand isentropically and work is extracted. Part of the work is used to drive the compressor and the remainder to produce power output which can be thrust or electricity based on the application.

2.1.2 The axial turbine

Central to the study, the axial turbine, comprises of fixed guide vanes and rotating blade rows. These are called stator and rotor respectively, which in conjunction form a stage. A typical gas turbine engine will have multiple stages with increasing radius to achieve high-power output and efficiency. The blades are mounted on a platform called hub and enclosed in a casing called shroud. In-between, lies the main annulus region. The primary purpose of the stator is acceleration and alignment of the flow for the rotor. And the rotor extracts work from the fluid by converting its kinetic energy into mechanical energy. In addition, the rotor also aligns the flow to subsequent stator.

2.1.2.1 Velocity triangles

The flow through a stage is traditionally studied through a radial schematic of the stage at a certain blade span as represented in Figure 2.2. These schematics are known as velocity triangles.

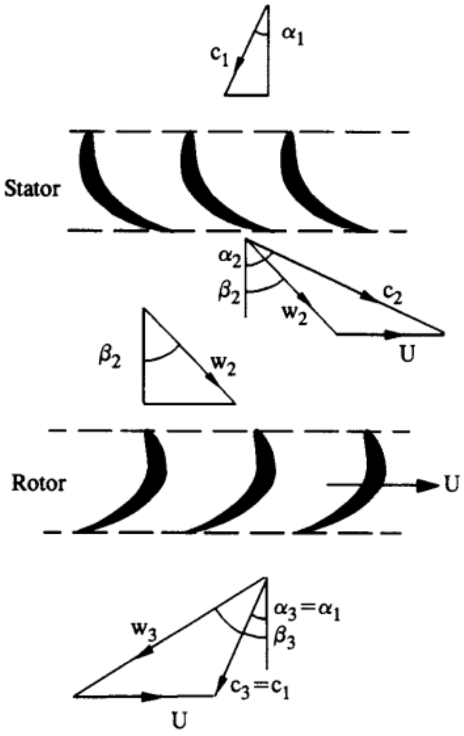

Figure 2.2: Velocity triangles for an axial turbine stage [3].

Here, the flow enters the stator from the top with a velocity c_1 at an angle α_1 and leaves at a higher velocity c_2 with an angle α_2 in the stationary frame of reference. As the rotor is rotating at a speed u , in relative terms, the flow enters the rotor at a velocity w_2 and angle β_2. The rotor, much like the stator, also redirects the flow producing an exit velocity $c_3 = c_1$ and angle $\alpha_3 = \alpha_1$ for the subsequent stator row. The absolute, relative and rotor blade speed are interrelated as in Equation 2.1.

$$c = w + u \tag{2.1}$$

It is also worth introducing here the meridional velocity, which is used to simplify the three-dimensional analysis by assuming the flow does not vary in the tangential direction. This meridional velocity is defined as in Equation 2.2.

$$c_m = \sqrt{c_x^2 + c_r^2} \tag{2.2}$$

where c_x and c_r denote axial and radial component of absolute velocity. For an axial flow machine, this is simplified to $c_m = c_x$.

2.1.2.2 Euler turbine equation

As the fast moving fluid is subjected to turning and momentum changes, it exerts a force on the blades and experiences a reactionary force from the blades. This is governed by Newton's II law of motion, given by

$$\sum F = \frac{d}{dt}(mc) \tag{2.3}$$

Since the turbine is mounted on a shaft, the fluid experiences torque which can be used to quantify power output from the turbine. Applying Equation 2.3 at rotor exit in circumferential direction (subscript θ) under constant massflow assumption,

$$\tau = \dot{m}(r_3 c_{3\theta} - r_2 c_{2\theta}) \tag{2.4}$$

Recognizing Ω as the angular velocity and u as a product of radial location and angular velocity ($u = \Omega r$) the rate of work done on the fluid is obtained. As the work is done by the fluid, appropriate sign convention is applied and we obtain Euler's turbine Equation 2.6.

$$\tau\Omega = \dot{m}\Omega(r_3 c_{3\theta} - r_2 c_{2\theta}) \tag{2.5}$$

$$W = u_2 c_{2\theta} - u_3 c_{3\theta} \tag{2.6}$$

This can also be written in terms of total enthalpy. As no work is extracted in stator the stagnation enthalpy remains constant ($h_{02} = h_{01}$) leading to equivalent form of Equation 2.6,

$$W = h_{01} - h_{03} \tag{2.7}$$

2.1.2.3 Turbine efficiency

Though the ideal assumption is useful for understanding, in reality there are losses associated in every step of the cycle. The Figure 2.3 shows the Pressure - Volume (P-V) on the left and Temperature - Entropy (T-S) diagram on the right for the Brayton cycle. In the latter, the curve $3 - 4'$ represent the ideal scenario and 3-4 the actual one. The losses can be attributed to an increase in entropy resulting in reduction of net usable work.

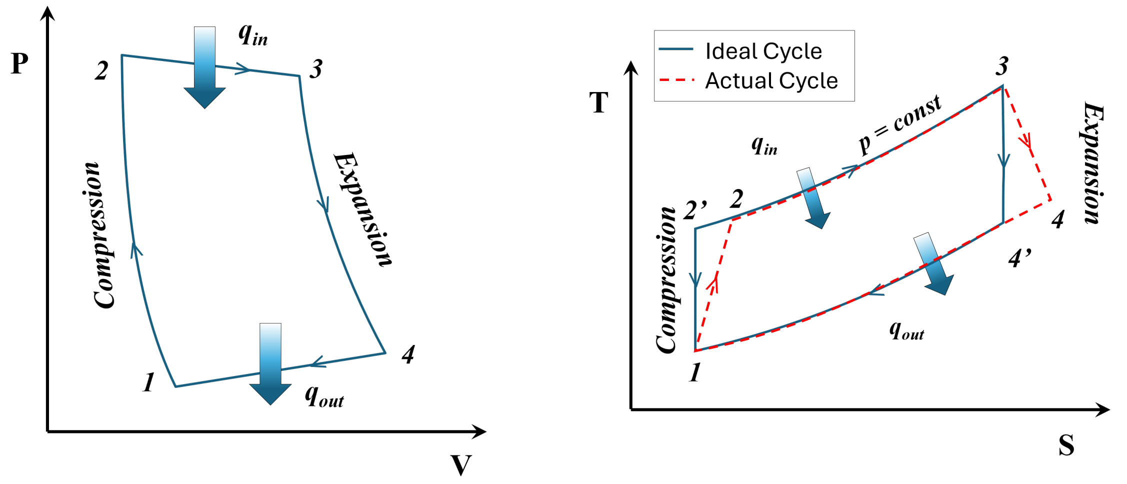

(a) P-V diagram

(b) T-S diagram

Figure 2.3: Ideal and actual Brayton cycle.

The performance of a turbine is quantified through efficiency. It is defined as the ratio of actual enthalpy change to isentropic enthalpy change. Two definitions of efficiency exist on the basis of kinetic energy utilization. If the kinetic energy is fully utilized, then total-to-total efficiency in Equation 2.8 is used.

$$\eta_{tt} = \frac{h_{01} - h_{03}}{(h_{01} - h_{03})_{isentropic}} \tag{2.8}$$

And when the kinetic energy is not utilized, total-to-static efficiency in Equation 2.9 is used. This efficiency is also used if the total conditions cannot be measured or is unreliable.

$$\eta_{ts} = \frac{h_{01} - h_{03}}{(h_{01} - h_{3})_{isentropic}} \tag{2.9}$$

Considering torque losses, the real enthalpy change can be formulated as follows [1]:

$$h_{01} - h_{03} = \frac{\Omega(\tau_{shaft} + \tau_{losses})}{\dot{m}} \tag{2.10}$$

For the isentropic part, assuming a calorically perfect gas, a relation can be derived as shown below, where κ is the ratio of specific heat.

$$(h_{01} - h_{03})_{isentropic} = c_p T_{01} \left(1 - \left(\frac{p_{03}}{p_{01}}\right)^{\frac{\kappa-1}{\kappa}}\right) \tag{2.11}$$

$$(h_{01} - h_{3})_{isentropic} = c_p T_{01} \left(1 - \left(\frac{p_{3}}{p_{01}}\right)^{\frac{\kappa-1}{\kappa}}\right) \tag{2.12}$$

2.1.2.4 Secondary Air Systems (SAS)

A closer look at the thermodynamic cycle in Figure 2.3b, suggests that a higher TET is linked to a higher efficiency. However, as stated earlier, this is limited by the material properties and sufficient cooling is required to protect the turbine. The SAS plays a vital role in the cooling process of turbine components. A typical schematic of SAS is shown in the Figure 2.4 where the red arrows represent the circulation of cooling air through the turbine components.

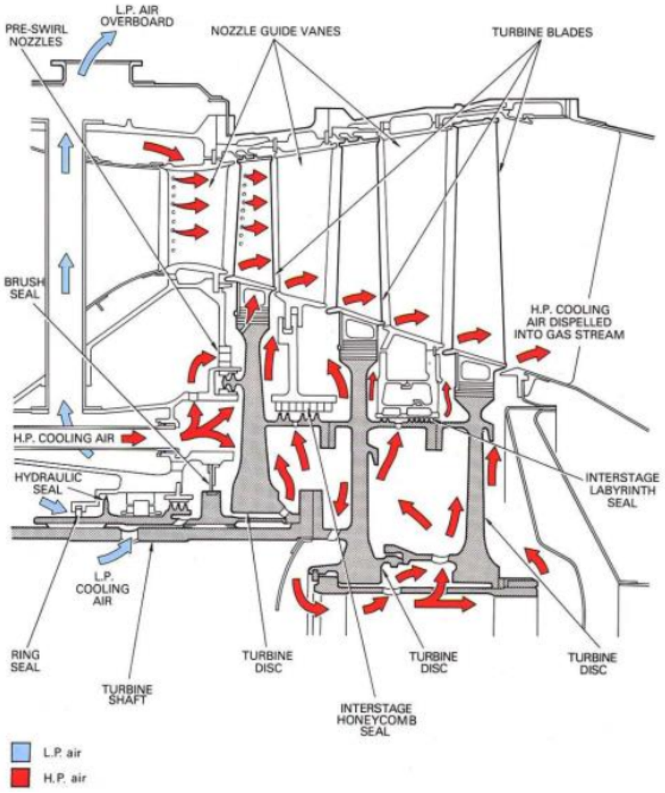

Figure 2.4: Schematic of SAS in a gas turbine [4].

About 20-30% of air from a suitable stage of compressor is directed to the SAS and utilized in cooling the blades exposed to high temperature. The pressurized air is also utilized in protecting the discs housing the stator and rotor, as well as the wheelspace cavity between them. This is yet another important function of SAS and the process is coined as *Cavity purge cooling* or *Purge cooling* and the coolant flow is called as *Purge flow*. The difference in density, owing to the inherent temperature difference between the two flows, forms a barrier which prevents the ingestion of hot gases. While the purge flow facilitates in cooling, it ultimately mixes with mainstream flow and exits through the rimseal into the main annulus. As the coolant flow is ejected into the mainstream, it enhances the secondary vortex structures resulting in overturning of the flow. This reduces the efficiency of the stage or in other words increases entropy. This increase in entropy has been quantified by Shapiro [15] using control volume approach and was found to be dependent on velocity, temperature, and angular difference between the two flows.

2.2 Rotor-stator wheelspace flow

The rotor-stator wheelspace comprises of rotating rotor disc and a stationary stator disc. The system operates on the principles of a rotating disc flow, and a recent consolidation of underlying physics is detailed by Childs [5].

2.2.1 Flow regimes

Through the work of Daily & Nece [16], four regimes have been identified in an enclosed rotor - stator wheelspace cavity as shown in Figure 2.5. These flow regimes are characterized by rotational Reynolds number (Re_θ) and gap ratio (G) defined by Equations 2.13 and 2.14 respectively. These regimes are:

1. Laminar flow, small clearance, merged boundary layers
2. Laminar flow, large clearance, separated boundary layers
3. Turbulent flow, small clearance, merged boundary layers
4. Turbulent flow, large clearance, separated boundary layers

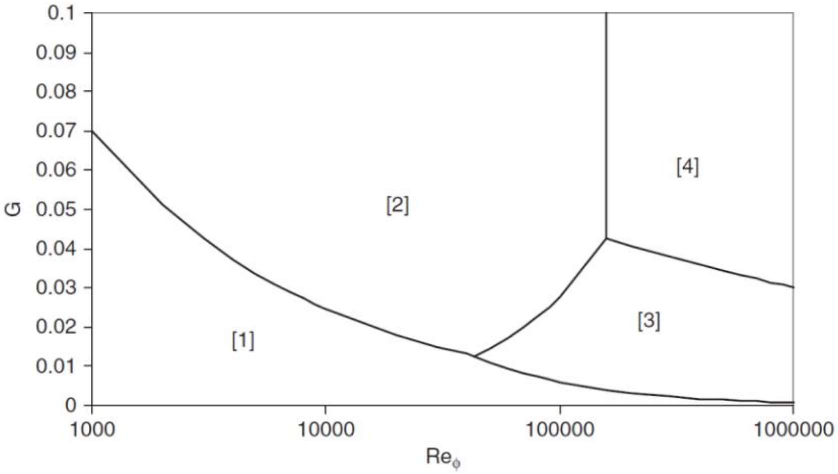

Figure 2.5: Flow regimes inside the wheelspace. Adopted from [5].

For the rotational Reynolds number, the speed is considered at the rotor periphery with hub radius b as characteristic length.

$$Re_\theta = \frac{\rho \Omega b^2}{\mu} \tag{2.13}$$

The gap ratio is defined as ratio of axial distance a of the cavity to hub radius.

$$G = \frac{a}{b} \tag{2.14}$$

The Figure 2.6 depicts these key dimensions. Here, s_c denotes axial seal clearance which is useful in characterizing rim seals.

$$G_c = \frac{s_c}{b} \tag{2.15}$$

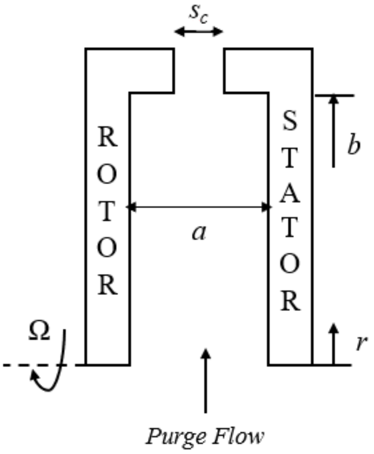

Figure 2.6: Key dimensions of wheelspace cavity.

2.2.2 Conceptual flow inside the wheelspace

In this thesis, the HPT wheelspace operates in the region 4 where the flow is turbulent and the boundary layers are separated. These boundary layers exist on either extreme of the cavity: the stator and the rotor discs, with an inviscid core in between. The flow inside such a system can be explained using Figure 2.7a. The high-temperature fluid entering the cavity is called *Ingress* while the purge flow ejected into the mainstream is called *Egress.*

The mainstream gas which potentially ingress into the cavity travels radially downwards on the stator wall and feeds the inviscid core. The inviscid core itself is axisymmetric and subject to axial flow which strengthens the rotor boundary layer. On the other end, the coolant flow entering from a lower radius is entrained to the rotor wall, providing most of its cooling to the rotor disc. As it moves radially upwards, it is fed by the inviscid core and gets diluted by the ingress. Finally, a part of the flow egress through the rim seal into main annulus and the remainder mixes with the ingress and travels through the stator wall. Thus, unlike the rotor boundary layer, the stator boundary layer loses its mass radially downwards. For comparison, a wheelspace operating in region 3 is shown in Figure 2.7b. In such cases as stated earlier, the boundary layers are merged and no inviscid core exists. Looking at the velocity distribution between the two regimes, the radial velocity in merged boundary layers passes through zero as it transitions from inflow to outflow whereas with separated boundary the transition occurs over a range. In this range, the axial velocity is maximum which indicating the existence of inviscid core. Additionally, a continuous tangential velocity gradient is observed in merged boundary regime while in the former, a constant plateau region is seen. The magnitude of velocity components in both cases are of the order $v_\theta > v_r > v_x$ but the distribution is not to scale, where v_θ is typically several orders of magnitude larger.

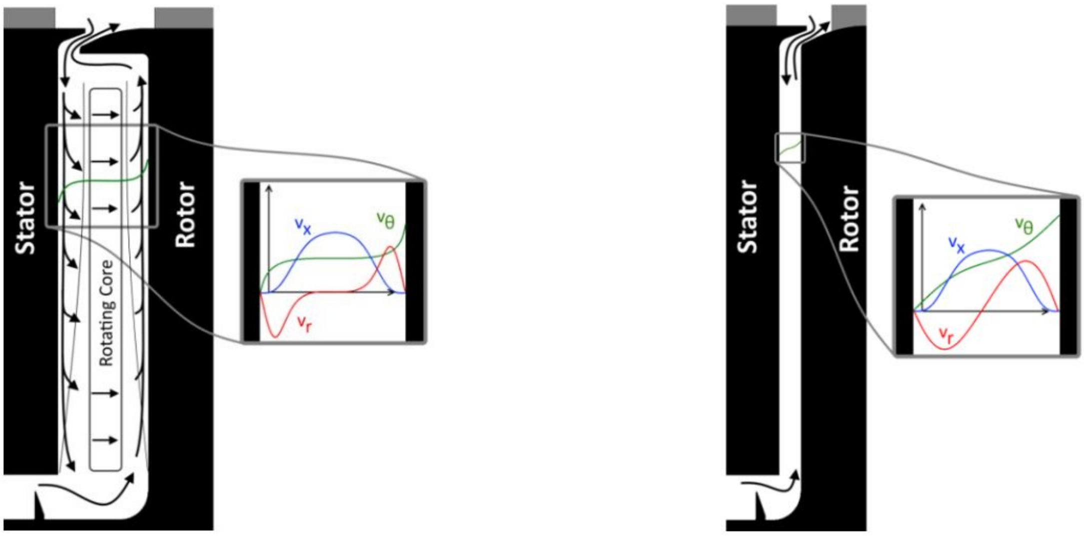

(a) **(b)**

Figure 2.7: Flow in wheelspace with (a) separated and (b) merged boundary layers [1].

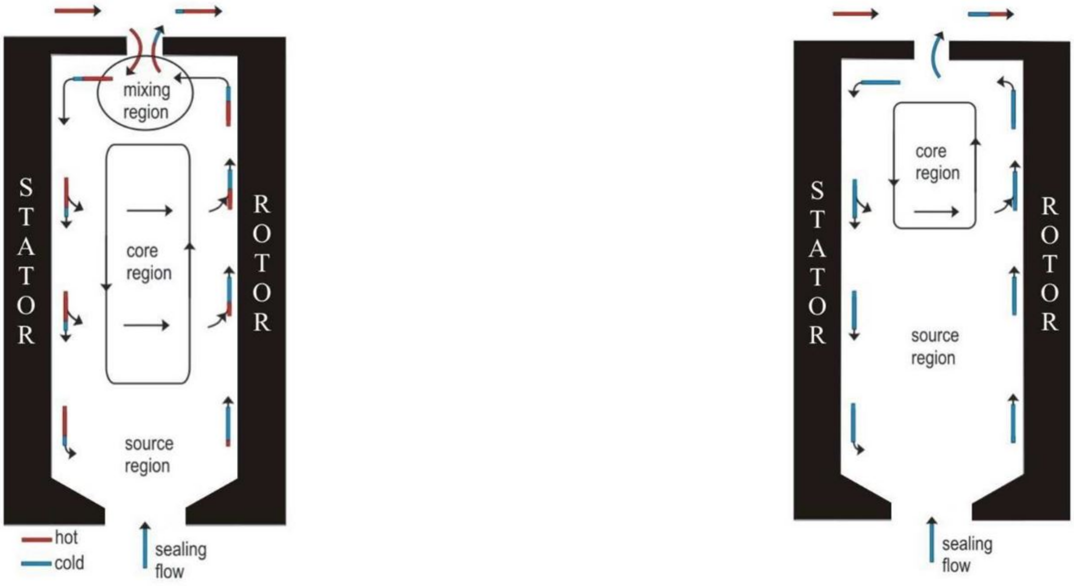

(a) **(b)**

Figure 2.8: Flow in the wheelspace for (a) $\Phi_o < \Phi_{min}$ and (b) $\Phi_o = \Phi_{min}$ [6].

The Figure 2.8 illustrates the same flow in region 4 with the superposed purge flow in blue and ingress in red for different non-dimensional purge flow rates Φ_o (defined in section 2.2.4.). There exists a minimum value Φ_{min} where the ingress is completely prevented, and when $\Phi_o = \Phi_{min}$ the core region is reduced in size and moves to a higher radius [1, 6].

2.2.3 Ingress driving mechanisms

While ingress has been referenced multiple times, the underlying mechanisms have not been formally discussed. Thus, it will be the focus of this section.

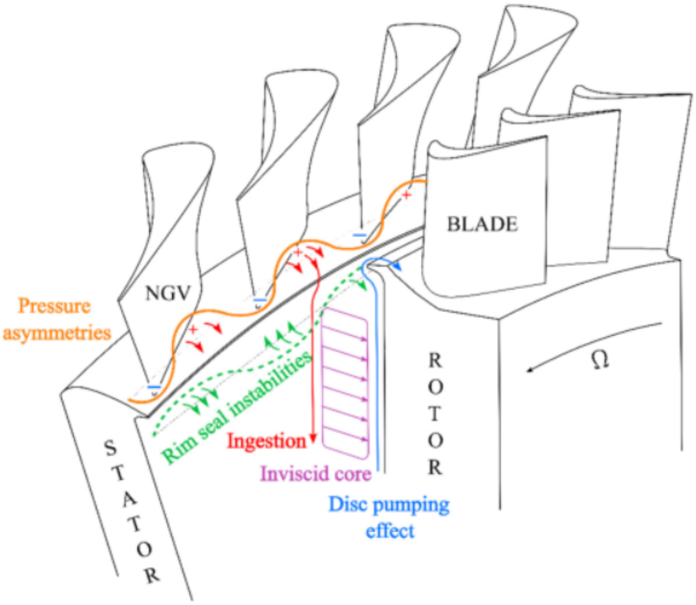

Figure 2.9: Hot gas ingress driving mechanisms [7].

The ingress driving mechanisms have not been fully understood but the research has identified two primary factors. These are: (i) Externally Induced (EI) ingress and (ii) Rotationally Induced (RI) ingress. The Figure 2.9 depicts the various ingress mechanisms.

2.2.3.1 Externally Induced (EI) ingress

The flow moving through pressure and suction sides of the vanes and blades create a tangential pressure asymmetry. Located at the interface of stator - rotor radially outward from the rim seal, they drive ingress and egress based on localized pressure difference between main annulus and cavity. This type of ingress is called EI ingress. If the local pressure is higher in the main annulus than the cavity, it leads to ingress and when the converse is true, it leads to egress [17]. In the Figure 2.9, the EI is identified by sinusoidal pressure asymmetries colored in orange.

2.2.3.2 Rotationally Induced (RI) ingress

Even when the pressure distribution in the mainstream flow is quasi-axisymmetric (i.e almost zero or zero circumferential variation), ingress still occurs due to the rotation of the rotor. The phenomenon is governed by the *disc pumping effect* [5] and illustrated in Figure 2.10.

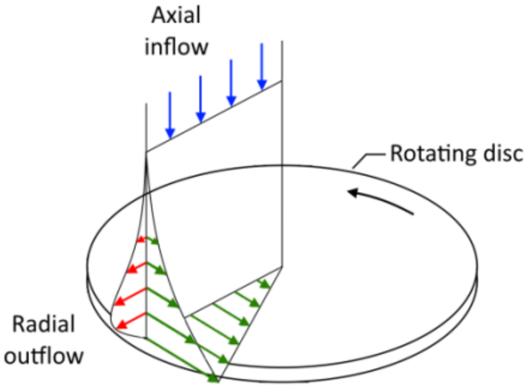

Figure 2.10: Disc pumping effect [5].

Since the coolant flow is entrained to the rotor boundary layer, closer to the disc surface it moves with the rotor due to no-slip condition. However, as we move away in the wall normal direction, the no-slip condition falls and the flow develops a radial component due to the centrifugal effects. This radial movement causes egress close to the rotor hub where the centrifugal effects are greatest. Therefore, to satisfy the mass imbalance inside the cavity, a radial inflow of ingress occurs. [18].

2.2.3.3 Combined Ingress (CI)

When the axial reynolds number (defined in Section 2.2.4) in the mainstream and the rotational reynolds number in the cavity are of similar magnitude both EI and RI contributes to ingress. This is called Combined Ingress (CI) and is predominant when the turbine is operated at off-design conditions and in double rim seal geometries. In the latter, for the inner seal RI dominates and for outer seal EI tends to dominate the ingress levels [17, 19].

2.2.3.4 Rim seal instabilities

The key objective is to minimize the purge - mainstream interaction. To achieve this objective, rim seals are usually employed on the hub periphery. Depending on the turbine various configurations exist and the common rimseal configurations are shown below in Figure 2.11.

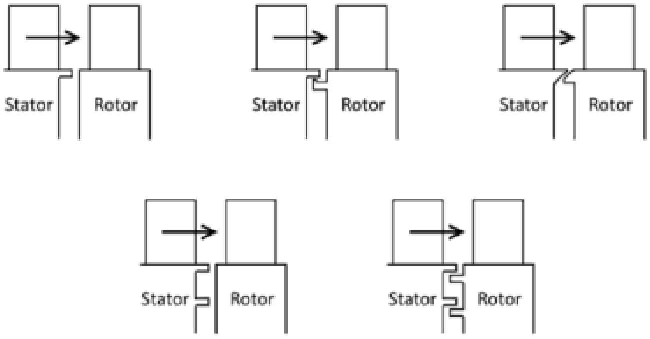

Figure 2.11: Common rim seal configurations [5].

The geometry of the rimseal itself can cause instabilities in the flow which can impact the degree of ingestion. However, evaluation of rimseal design is not the focus of this study. The HPT involved in this thesis use a chute seal which can be identified on the top right in the Figure 2.11.

Apart from these mechanisms, flow inside the wheelspace can also suppress or exacerbate ingress. Large-scale flow structures, shown in figure 2.12, move at lower speed than that of blade and were first identified by Cao et al., [8]. Their work, included both experimental and computational analysis. The computational domain in the analysis did not include vanes nor blades and used 90° and 360° models. It was found that these structures are difficult to capture in smaller sector models. The sound argument for the physical origin of these structures is attributed to Kelvin-Helmholtz instabilities [9] and Taylor-Couette flows [20].

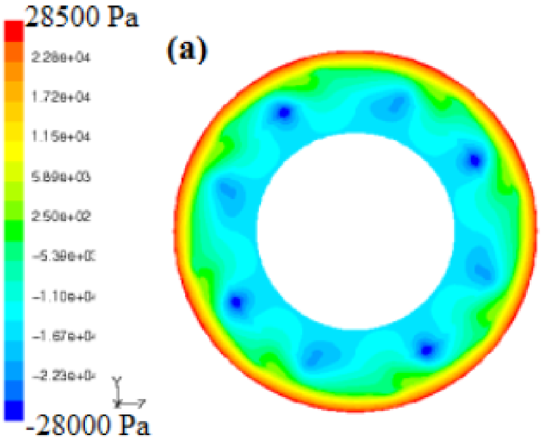

Figure 2.12: Large scale flow structures inside cavity - 90° sector model [8].

2.2.3.5 Kelvin-Helmholtz instabilities

The Kelvin-Helmholtz (K-H) instabilities are formed at the meeting point of these purge - mainstream flow. The formation of these vortices can be understood with the help of Figure 2.13. If we assume the two fluids are separated by an infinitely thin vortex street with uniform vorticity, then any small perturbation will create a localized pressure difference resulting in the formation of larger vortex sheets over time. These vortex sheets are unsteady and differ in their length scales.

In the wheelspace cavity, due to the tangential velocity difference between the purge and mainstream flow, large vortex sheets are developed over time and drive ingress deeper into the cavity [9].

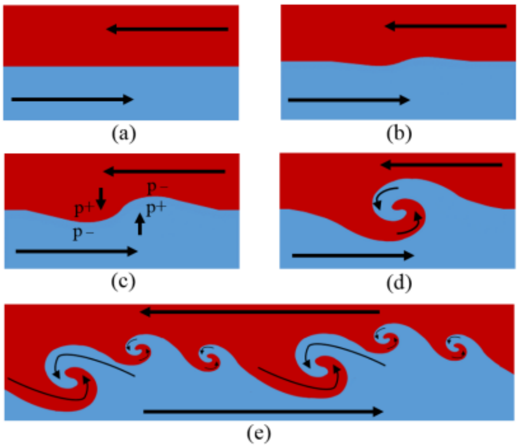

Figure 2.13: Formation of Kelvin - Helmholtz vortical structures [9].

2.2.3.6 Taylor-Couette flows

As stated earlier, the wheelspace cavity comprises of a stationary stator wall and rotating rotor wall. This can be simplified to a taylor-couette system as in Figure 2.14. When the pressure gradient between main annulus - cavity and the centrifugal force due to rotor compete, especially at high speeds, this structures can become unstable and drive ingestion to the cavity. These instabilities are another argument used to interpret the formation of large scale flow structures which may drive ingress of hot gas into the cavity.

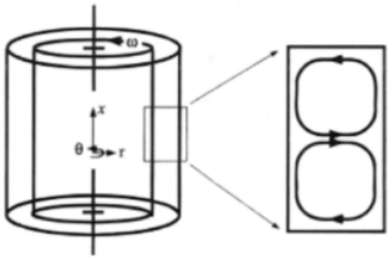

Figure 2.14: Taylor-Couette instability [10].

2.2.4 Non-dimensional coefficients

Since the geometry of the wheelspace differ between turbines, non-dimensional coefficients are useful in correlation of results. The non-dimensional coefficients relevant to this thesis are defined below. For, the unknown parameters refer to the Nomenclature.

1. Axial Reynolds number - represents the Reynolds number in the main annulus.

$$Re_{c_x} = \frac{\rho c_x b}{\mu} \tag{2.16}$$

2. Rotational Reynolds number - redefined from Equation 2.13 for reading continuity.

$$Re_\theta = \frac{\rho \Omega b^2}{\mu}$$

3. Flow coefficient - it is defined as the ratio of axial and rotational reynolds number

$$C_f = \frac{Re_{c_x}}{Re_\theta} \tag{2.17}$$

4. Non-dimensional cavity mass flow - a non dimensional value which represents the purge mass flow rate.

$$C_w = \frac{\dot{m}}{\mu b} \tag{2.18}$$

5. Seal clearance ratio - redefined from Equation 2.15 for reading continuity.

$$G_c = \frac{s_c}{b} \tag{2.19}$$

6. Non-dimensional sealing parameter - an important non-dimensional parameter useful for reproducing results for scaled geometries and for different operating speeds.

$$\Phi = \frac{C_w}{2\pi G_s Re_\theta} \tag{2.20}$$

   Alternatively can be represented as below,

$$\Phi = \frac{U}{\Omega b} \tag{2.21}$$

   where U is the mean flow velocity through the rim seal geometry formulated as,

$$U = \frac{\dot{m}}{2\pi \rho b s_c} \tag{2.22}$$

7. Sealing effectiveness - quantifies the performance of the rim seal and used to estimate ingress levels. Experimentally, this quantity can be evaluated by introducing a non-reacting seed gas. The concentration of the seed gas can then be tracked to evaluate sealing effectiveness at various locations using the Equation 2.23.

$$\varepsilon = \frac{\gamma_s - \gamma_{inlet}}{\gamma_o - \gamma_{inlet}} \tag{2.23}$$

where γ_s - concentration at a radial location, γ_o - seed gas concentration at purge inlet and γ_{inlet} - ambient seed gas concentration.

An equivalent expression exists in terms of non-dimensional sealing parameter Φ as in Equation 2.24.

$$\varepsilon = 1 - \frac{\Phi_i}{\Phi_e} = \frac{\Phi_o}{\Phi_o + \Phi_i} \tag{2.24}$$

where $\Phi_o = \Phi_e - \Phi_i$ and subscripts 'o' refers to the amount of purge flow and 'i' refers to ingress amount and 'e' refers to egress amount.

2.3 Computational Fluid Dynamics (CFD)

Analysis of fluid flow, heat and other associated systems through computer based simulations involves usage of CFD principles. The basis of CFD is dictated by three equations also called governing equations. These are:

1. Mass conservation - continuity equation
2. Momentum conservation - Navier Stokes equation
3. Energy conservation - energy equation

For an incompressible flow, the continuity and Navier Stokes equations can be written as in Equation 2.25, 2.26 respectively. The energy equation is of little relevance to the thesis and hence not discussed.

$$\frac{\partial v_i}{\partial x_i} = 0 \tag{2.25}$$

$$\rho \frac{\partial v_i}{\partial t} + \rho \frac{\partial v_i v_j}{\partial x_j} = -\frac{\partial p}{\partial x_i} + \mu \frac{\partial^2 v_i}{\partial x_j \partial x_j} \tag{2.26}$$

Based on the finite volume approach, the computational domain is split into cells of finite volumes. For each volume, the complex governing equations are discretized, solved and finally integrated to provide the solution for the whole domain. The number of unknown parameters are more than number of equations therefore an iterative approach is required. The flows encountered in gas turbines are highly turbulent which makes solving the governing equations all the more complex. The following sections are a summary based on the detailed knowledge found in [21].

2.3.1 RANS

One approach in turbulence modeling involves decomposing the instantaneous variable value into a mean and fluctuating parts as below,

$$v_i = \overline{v_i} + v_i^{'} \qquad p = \overline{p} + p^{'} \tag{2.27}$$

where the mean values are averaged over a sufficiently large period of time. The averaging is defined as,

$$\overline{v} = \frac{1}{2T}\int_{-T}^{T} v dt \tag{2.28}$$

This approach leads to formulation of Reynolds Averaged Navier- Stokes (RANS) equations.

$$\frac{\partial \overline{v_i}}{\partial x_i} = 0 \tag{2.29}$$

$$\underbrace{\frac{\partial \overline{v}_i \overline{v}_j}{\partial x_j}}_{\mathit{Convection}} = \underbrace{-\frac{1}{\rho}\frac{\partial \overline{p}}{\partial x_i}}_{\text{Pressure Gradient}} + \underbrace{\nu \frac{\partial^2 \overline{v}_i}{\partial x_j \partial x_j}}_{\mathit{Diffusion}} \underbrace{-\frac{\partial \overline{v_i^{'} v_j^{'}}}{\partial x_j}}_{\text{Stress Tensor}} \tag{2.30}$$

Notice that on comparison to 2.26 the first term has been dropped. This is because the RANS equations is time independent and all of the turbulence is modeled. While RANS equations are computationally cheap and robust, they fail to capture the physics of strong unsteady flows.

2.3.2 URANS

The Unsteady RANS (URANS) formulation allows takes the time dependant changes into account and to a certain extent resolves the turbulent fluctuations. The averaging in URANS can be defined as in Equation 2.31. Here, an requirement arises where the timestep t should be smaller than timescale of turbulence structures.

$$\overline{v}(t) = \frac{1}{2T}\int_{t-T}^{t+T} v(t) dt \tag{2.31}$$

This results in variable decomposition as in Equation 2.32. And even though the results are unsteady the interest lies in time averaged value $\overline{v}_i$.

$$v_i = \overline{v_i} + v_i^{'} = \langle \overline{v}_i \rangle + \overline{v_i^{'}} + v_i^{''} \quad ; \quad \overline{v_i} = \langle \overline{v}_i \rangle + \overline{v_i^{'}} \tag{2.32}$$

where $\langle \overline{v}_i \rangle$ is the time averaged value similar to RANS, $\overline{v_i^{'}}$ is time averaged resolved fluctuation and $v_i^{''}$ is the modeled fluctuation. The governing equations now include the transient term as below,

$$\underbrace{\frac{\partial \overline{v}_i}{\partial t}}_{\mathit{Transient}} + \underbrace{\frac{\partial \overline{v}_i \overline{v}_j}{\partial x_j}}_{\mathit{Convection}} = \underbrace{-\frac{1}{\rho}\frac{\partial \overline{p}}{\partial x_i}}_{\text{Pressure Gradient}} + \underbrace{\nu \frac{\partial^2 \overline{v}_i}{\partial x_j \partial x_j}}_{\mathit{Diffusion}} \underbrace{-\frac{\partial \overline{v_i^{''} v_j^{''}}}{\partial x_j}}_{\text{Stress Tensor}} \tag{2.33}$$

The decomposition of the variables in both RANS and URANS formulation introduce a new stress tensor or reynolds stress tensor term as denoted in equation 2.33. This term represents correlation between fluctuating velocities and require a model to close the system. This leads to the turbulence closure problem and various turbulence models are employed depending on the case to solve the problem.

Before introducing these models. certain non dimensional parameter important for accuracy of CFD solutions are introduced.

1. **Wall $\mathbf{y^+}$**: An important parameter which represents the first cell thickness. A sufficiently low value is necessary to ensure boundary layer is properly modeled.

   $$y^+ = \frac{y\sqrt{\tau_{wall}/\rho}}{\nu} \tag{2.34}$$

   It represents the thickness of first cell near the wall. It is important to achieve a sufficiently low value to ensure the boundary layer is captured over many cells and modeled properly.

2. **CFL number**: The Courant-Friedrichs-Lewy (CFL) number determines the stability and accuracy of transient simulations. It is defined as below,

   $$CFL = \frac{v\Delta t}{\Delta x} \tag{2.35}$$

   If the flow structures evolve faster than the chosen timestep, it will not be resolved and leads to erroneous or divergence issues. The CFL should be sufficiently small, ideally 1, in the computational domain to ensure accurate and stable results.

2.3.3 Shear Stress Transport (SST) $k - \omega$ model

The SST $k - \omega$ is a two-equation turbulence model based on $k - \epsilon$ and $k - \omega$. The $k - \epsilon$ performs well in the freestream region but over predicts shear stress in adverse pressure regions and requires near wall modifications. Conversely, the $k - \omega$ is accurate in the near wall region but is dependent of free stream value of specific dissipation. By combining both these models through blending functions, an improved model, SST $k - \omega$, is formulated. According to the model, $k - \omega$ is employed in adverse pressure gradient regions and $k - \epsilon$ in the freestream zones. This improved model accounts for turbulent shear stress and accurately predicts the onset and amount of flow separation under adverse pressure gradients [22].

Gas turbine flow involve significant swirling and areas of adverse pressure gradients which makes this model a perfect fit. The mathematical formulation of this model is as follows, Turbulent kinetic energy (k) equation :

$$\frac{\partial k}{\partial t} + \frac{\partial}{\partial x_j}\left(\overline{v}_j k\right) = \frac{\partial}{\partial x_j}\left[\left(\nu + \frac{\nu_t}{\sigma_k}\frac{\partial k}{\partial x_j}\right)\right] + P^k - \beta^* k\omega \tag{2.36}$$

Specific dissipation (ω) equation:

$$\frac{\partial \omega}{\partial t} + \frac{\partial}{\partial x_j}\left(\overline{v}_j \omega\right) = \frac{\partial}{\partial x_j}\left[\left(\nu + \frac{\nu_t}{\sigma_\omega}\frac{\partial \omega}{\partial x_j}\right)\right] + P^\omega - \beta\omega^2 + \frac{2(1-F_1)\sigma_{w2}}{w}\frac{\partial k}{\partial x_i}\frac{\partial \omega}{\partial x_i} \tag{2.37}$$

Here, the first blending function F_1 determines the switch between two models. $F_1 = 0 \implies k - \epsilon$ and $F_1 = 1 \implies k - \omega$. For intermediate values, the model is actively blending both formulation to ensure a smoother transition.

2.3.4 Stress Blended Eddy Simulation (SBES)

The SBES is a hybrid model which combines the advantage of Large Eddy Simulation (LES) and RANS. The core concepts revolves around resolving large turbulent eddies using LES and modeling small isotropic scales using RANS, where LES would be expensive. This switch is achieved using blending or shielding functions whose definition varies for each hybrid model. SBES is developed by Menter [23] and is an extension of Shielded Detached Eddy Simulation (SDES), another hybrid model. The current version of SBES in Ansys CFX, is restricted to SST $k - \omega$ for RANS part and Wall Adapting Local Eddy viscosity (WALE) LES for the LES half [24].

The involved equations are highly mathematical and complex. Therefore to prevent a cumbersome theory section, a brief summary is provided below. For detailed information, it is recommended to refer to [21, 24].

2.3.4.1 Concept of LES

The concept of LES can be understood with the help of Figure 2.15. Here, the largest eddies which span over a range of grid cells are resolved whereas the sub grid scales requires Sub-Grid Scale (SGS) models.

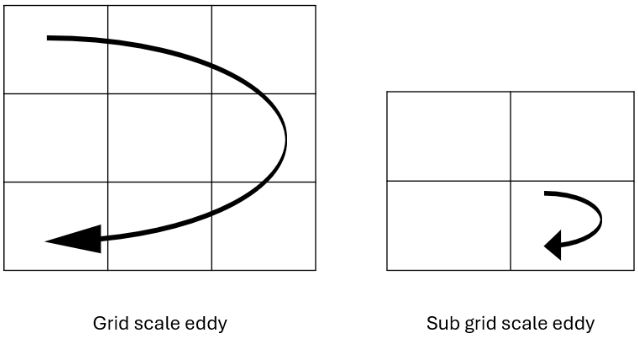

Figure 2.15: Representation of a large and a sub grid scale eddy.

In order to resolve the largest eddies, an averaging by volume is carried out. This averaging function in 1D can be written as in Equation 2.38. Note that the variables are function of space and time.

$$\tilde{\Phi}(x,t) = \frac{1}{\Delta x}\int_{x-0.5\Delta x}^{x+0.5\Delta x} \Phi(\xi,t)d\xi \tag{2.38}$$

which yields the spatially-filtered Navier-Stokes equation as follows,

$$\frac{\partial \tilde{v}_i}{\partial t} + \frac{\partial \tilde{v}_i \tilde{v}_j}{\partial x_j} = -\frac{1}{\rho}\frac{\partial \tilde{p}}{\partial x_i} + \frac{\partial}{\partial x_j}\left((\nu + \nu_{sgs})\frac{\partial \tilde{u}_i}{\partial x_j}\right) \tag{2.39}$$

where the ν_{sgs} denotes the SGS turbulent stresses.

2.3.4.2 WALE LES

Various closure models exist for the SGS. One such model is WALE SGS which defines as in Equation 2.40 where L_s is the mixing-length and S_{ij} is the strain rate tensor.

$$\nu_{SGS_{WALE}} = L_s^2 \frac{(S_{ij}^d S_{ij}^d)^{3/2}}{(\tilde{S}_{ij}^d \tilde{S}_{ij}^d)^{5/2} + (S_{ij}^d S_{ij}^d)^{5/4}} \tag{2.40}$$

2.3.4.3 Shielding in SBES

For hybrid models, the last term on the right hand side of Equation 2.36 is modified. For SDES this modification is as follows,

$$\beta^* k\omega \rightarrow \beta^* k\omega F_{SDES}$$

where the function F_{SDES} is defined as in Equation 2.41.

$$F_{SDES} = \left[max\left(\frac{L_t}{C_{SDES}\Delta_{SDES}}(1 - f_{SDES}), 1\right) - 1\right] \tag{2.41}$$

where L_t is turbulent length scale (Equation 2.42), C_{SDES} is an empirical value and Δ_{SDES} is mesh length scale (Equation 2.43) and f_{SDES} is the shielding function. The formulation of shielding function f_{SDES} is proprietary to Ansys and hence not disclosed.

$$L_t = k^{3/2}/\epsilon \tag{2.42}$$

$$\Delta_{SDES} = max(\sqrt[3]{V}, 0.2\Delta_{max}) \tag{2.43}$$

In SBES, this shielding function is explicitly included to the turbulence stress tensor as in Equation 2.44 which for eddy-viscosity based concepts can be simplified to Equation 2.45.

$$\tau_{ij}^{SBES} = f_{SDES}\tau_{ij}^{RANS} + (1 - f_{SDES})\tau_{ij}^{LES} \tag{2.44}$$

$$\nu_{t_{SBES}} = f_{SDES}\nu_t^{RANS} + (1 - f_{SDES})\nu_t^{LES} \tag{2.45}$$

3

Methodology

In this chapter, the pre-processing methodology and the CFD simulation setup are described in detail.

3.1 Meshing process

The HPT stage comprised of 42 stator blades (vanes) and 49 rotor blades (blades) and a model of the stage was provided by Siemens Energy (SE). In addition, the mesh for the vane geometry was also supplied. Hence only the blade and wheelspace cavity were meshed.

Prior to meshing a few pre-processing adjustments were carried out using in-house tools and Siemens NX to stitch geometry together. For meshing, NUMECA Autogrid 5^{TM} - a software developed specifically for turbomachinery was selected. A 3D structured grid was created using hexahedron cells. Except for the rotor-stator interface and the blade tip gap region, the grid is fully conformal. This ensures the solution is free of interpolation errors. For mesh studies, a total of three meshes of varied refinement levels were produced. This refinement was mainly focused on the cavity region. For all three meshes, metrics such as skewness and expansion ratio were evaluated. The Table 3.1 contains the details of these parameter for all the generated meshes.

Metric	**Coarse mesh**	**Base mesh**	**Fine mesh**
Element count	4.89×10^6	6.13×10^6	8.8×10^6
First cell thickness	$4.0 \times 10^{-6} m$	$3.0 \times 10^{-6} m$	$2.0 \times 10^{-6} m$
Min. skewness (Cavity)	26°	28°	27.2°
Expansion ratio (Cavity)	1.2	1.2	1.1

Table 3.1: Quality metrics for all meshes.

The skewness and expansion ratio mentioned in this Table 3.1 is considering the cavity. For the blade, due to the complex geometry of the hub fillet, few cells had a skewness of 15° and the expansion ratio was increased to save computational time. The Figure 3.1 depicts various regions of the mesh.

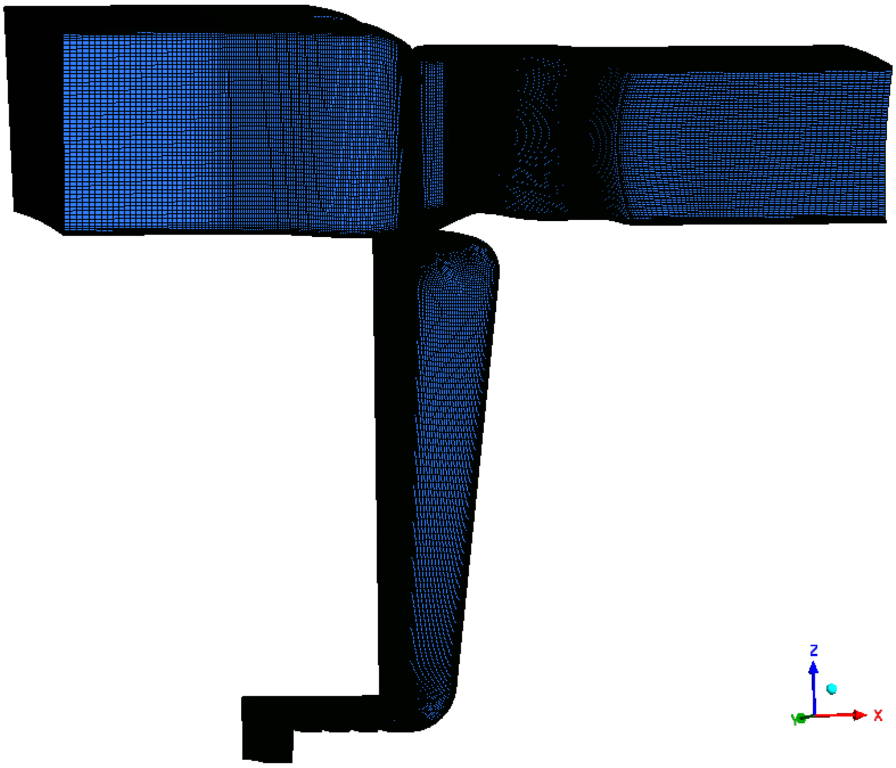

(a) Volume mesh

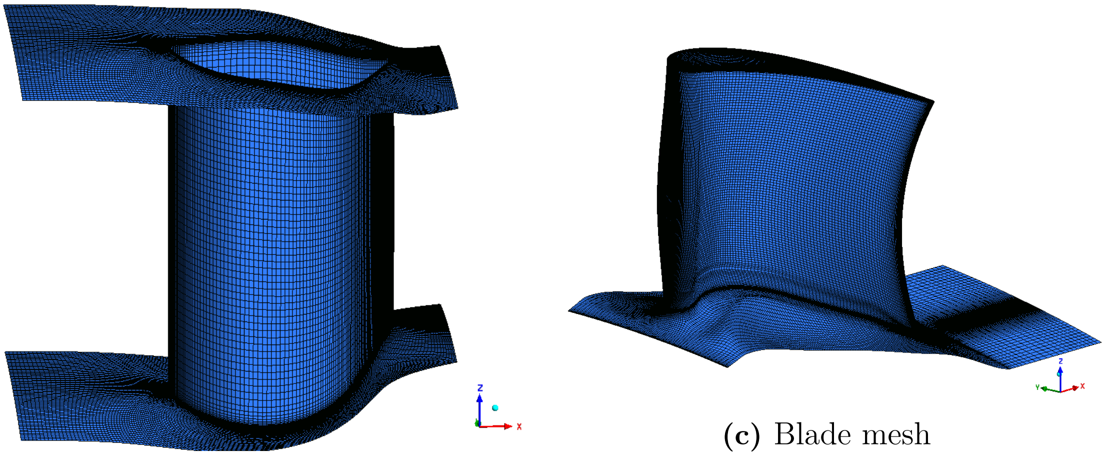

(c) Blade mesh

(b) Vane mesh

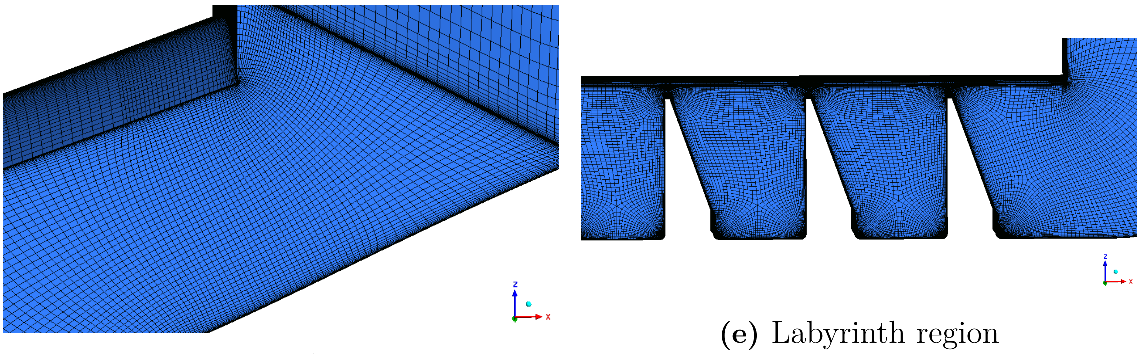

(e) Labyrinth region

(d) Rim seal region.

Figure 3.1: Illustration of 3D mesh.

3.2 Simulation setup

The simulations are carried out using Ansys CFX v2022 R2, a CFD code developed for turbomachinery analysis.

3.2.1 Computational domain

The analysis is carried out for two computational domains. These are:

- Single passage domain (SP domain): This domain comprised of 1 Vane, 1 Blade and the wheelspace cavity as shown in Figure 3.2a.
- Multi passage domain (Sector domain): A Sector domain comprising of 6 Vanes, 7 Blades with the wheelspace cavity. This Sector represents about 51° of the full 360° annulus as shown in Figure 3.2b.

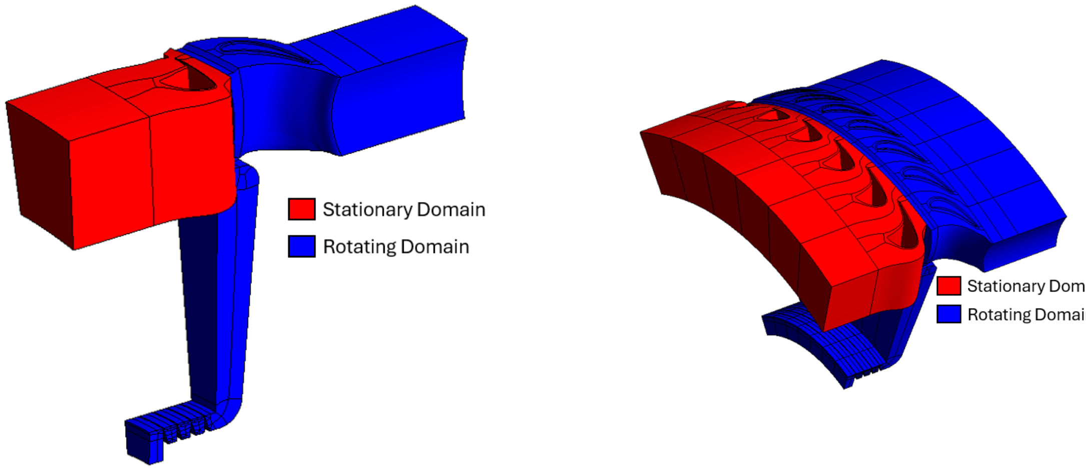

(a) **(b)**

Figure 3.2: Stage domains for CFD analysis. (a) SP domain (b) Sector domain

For both domains, the vane is defined under stationary frame and the blade including cavity is defined in a rotating frame of reference. The Sector model has a pitch ratio of 1, defined by Equation 3.1, required 6 vanes and 7 blades plus the wheelspace cavity. This Sector domain is created through rotational transformation of the SP domain. The former had a cell count of 52×10^6 and the latter had a total of 7.9×10^6 cells for the base mesh.

$$PR = \frac{N_{V,Sec}/N_V}{N_{B,Sec}/N_B} \tag{3.1}$$

3.2.2 Thermodynamic properties

The model comprised of two gases which are the main-annulus gas (hot gas): Air, and the cold purge gas (cold gas): Air (DR =1) and Argon (DR =1.38). The Air is modeled as an ideal gas with CFX's inbuilt properties. While for Argon, the required thermodynamic properties were obtained using SE database and imported into CFX. These properties are plotted below in Figure 3.3.

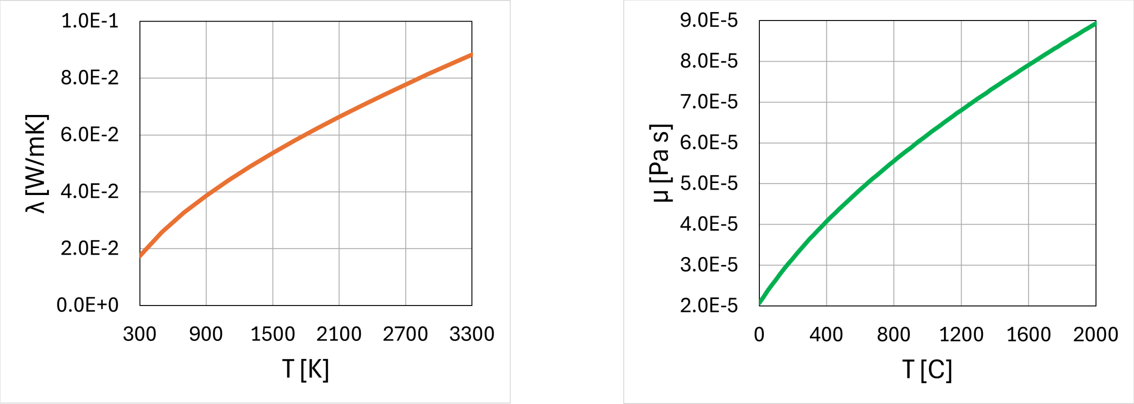

(a) Thermal conductivity λ [W/mK].

(b) Dynamic viscosity μ [Pa·s].

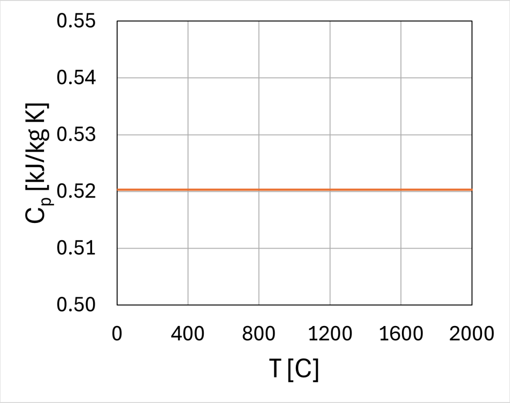

(c) Specific heat at constant pressure C_p [kJ/kg·K].

Figure 3.3: Thermodynamic properties of Argon (DR = 1.38) as a function of temperature.

3.2.3 Boundary conditions

The boundary conditions for both SP and Sector models remain similar with values adjusted according to the Sector size. In Ansys CFX, multiple gases can be introduced in the domain by defining them as a component mixture. Here, the main inlet gas : Air and the purge inlet gas: Air / Argon are defined as an ideal mixture. And by controlling the mass fraction, required gas is allowed at the corresponding inlets. All the walls are adiabatic and subject to no-slip condition. For the rotating domain, the RPM is 10540. Other conditions are described below with the help of Figure 3.4.

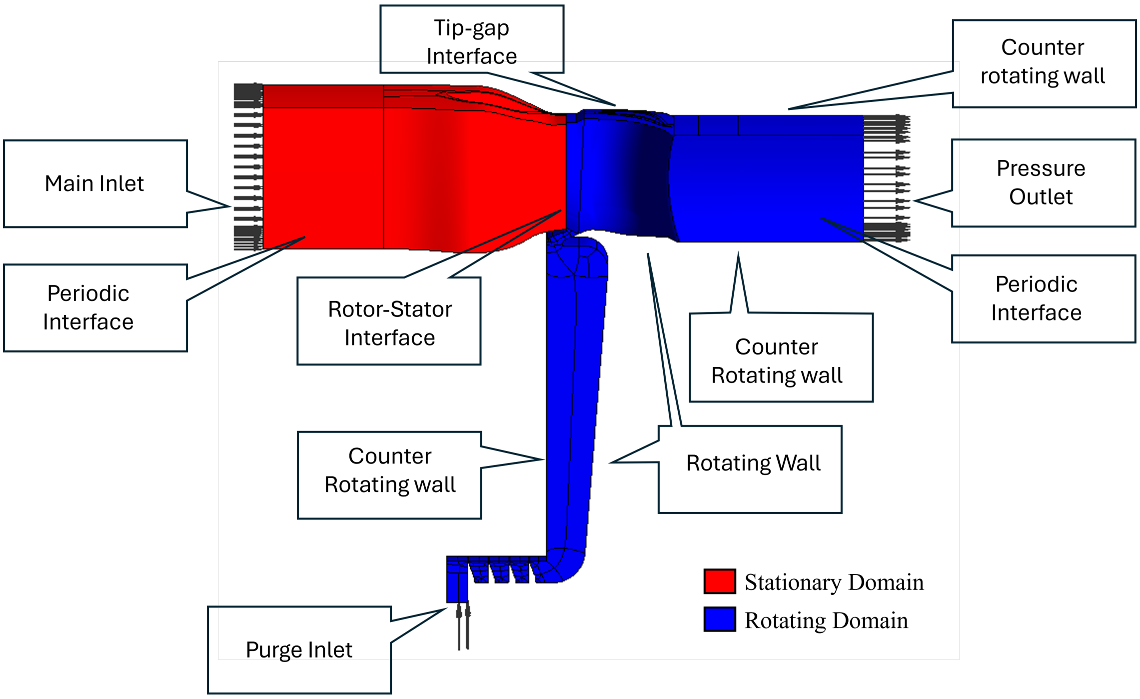

Figure 3.4: Domain boundary conditions.

- **Main inlet:** This is the inlet to the HPT stage where hot gas enters the domain. The flow components are fully axial with total pressure, total temperature, turbulence intensity, turbulence length scale and mach number defined using the experimental data. The Figure 3.5 below shows the normalized total pressure profile for the inlet.

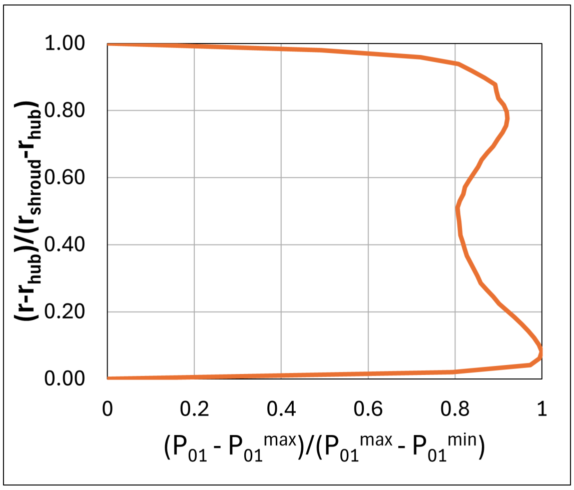

Figure 3.5: Normalized radial pressure profile at the main inlet.

- **Purge inlet:** The inlet where purge gas is introduced. It is a stationary inlet with purge gas mass flow, turbulence intensity and total temperature values defined. The purge gas enters radially and the mass flow for SP and Sector models are calculated based on Equation 3.2 and 3.3 respectively.

$$(\dot{m}_p)_{SP} = \dot{m}_{out} * \frac{42}{49} * MFR \tag{3.2}$$

$$(\dot{m}_p)_{Sector} = \dot{m}_{out} * MFR \tag{3.3}$$

- **Pressure outlet:** A stationary outlet of the HPT stage with atmospheric pressure conditions.
- **Rotating wall:** As the name suggests, these walls rotates at a defined speed of 10540 RPM. This condition is set for the disc and blade of the rotor row.
- **Counter rotating wall:** The stator disc, shroud, and extended hub boundaries are stationary walls. Since they lie within a rotating domain, this option ensures they remain static in the global frame of reference.
- **Periodic interface:** This conformal interface enforces rotational periodicity to represent the full 360° of the annulus.
- **Rotor-stator interface:** This interface connects the stator and rotor rows with a suitable rotor-stator model (refer Section 3.2.4). The mesh cells at this interface are non-conformally mapped.
- **Tip gap interface:** This interface connects the gap between the rotor blade and the casing shroud. Here, the mesh mapping is again non-conformal.

3.2.4 Solver settings

3.2.4.1 Steady state

The solver settings are listed in the Table 3.2 below. Ansys CFX uses pseudo-timescale approach in steady simulations. This *Auto timescale* option dynamically calculates a timescale based on global flow parameters and boundary conditions. And the high resolution scheme dynamically decides between first-order upwind and a high order methods based on the local flow conditions [22].

Parameter	**Setting**
Turbulence model	SST $k-\omega$
Rotor-stator interface	Mixing plane
Advection scheme	High resolution
Turbulence numerics	High resolution
Psuedo timescale control	Auto timescale

Table 3.2: Solver settings for steady state

3.2.4.2 URANS

Apart from the settings of steady state, for the URANS the following settings/changes in Table 3.3 were included. The timestep is based on the flowthrough time calculated using steady state results. Then an estimate of 50 timesteps per blade passage was decided. The transient rotor-stator basically rotates the rotor by dividing the time for a revolution to the set timestep.

Parameter	Setting
Rotor-stator interface	Transient rotor-stator
Transient scheme	Second order backward euler
Timestep	2.32×10^{-6} s
Iterations/timestep	10

Table 3.3: Solver settings for URANS

3.2.4.3 SBES

The modifications for the SBES are listed below in Table 3.4. The bounded central-differencing scheme is selected based on guidelines provided by Ansys for SRS cases [24].

Parameter	Setting
Advection scheme	Bounded central-differencing
Iterations/timestep	6

Table 3.4: Solver settings for SBES.

3.3 Estimation of sealing effectiveness (ε) in CFD

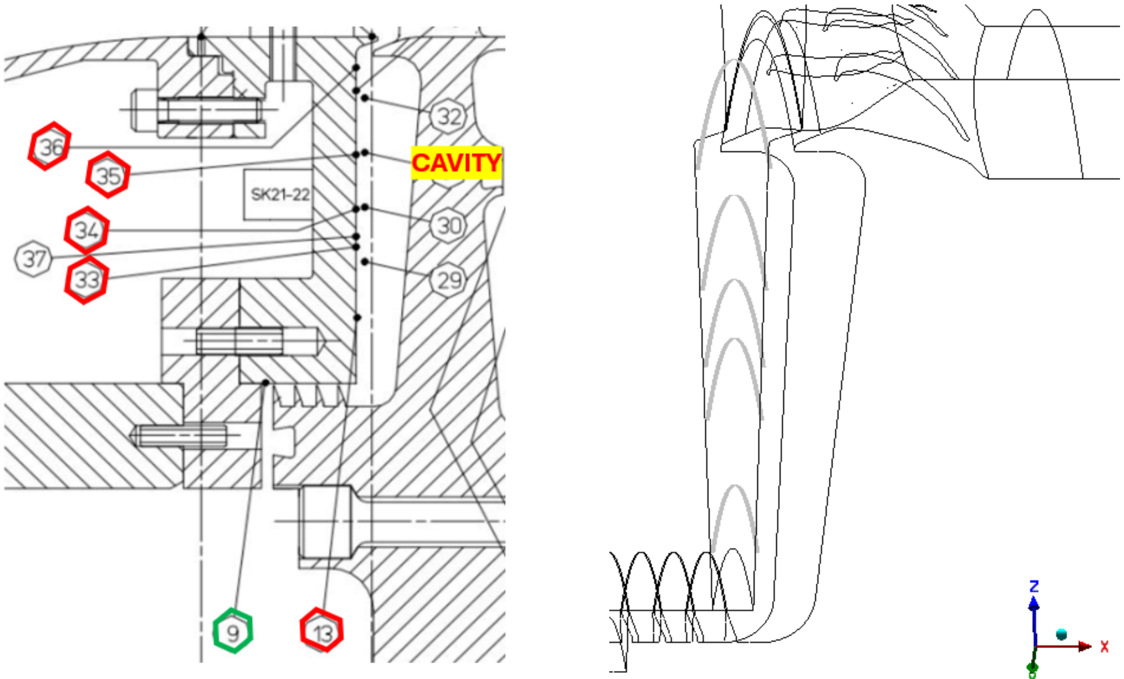

(a) Experimental probe locations. Adopted from [11].

(b) Equivalent CFD ribbons close to stator wall.

Figure 3.6: Sealing effectiveness measurement locations.

As previously mentioned in Section 2.2.4, sealing effectiveness (ε) can be estimated with the help of a non-reacting seed gas. Such an estimation utilizes the concentration based formulation as in Equation 2.23. This was adopted in the experimental work [11] and the Figure 3.6a shows the probe locations where these measurements were made. The probes highlighted in red measure local seed gas concentration γ_s while the one in green measure concentration at the purge inlet γ_0. On the right in Figure 3.6b, an equivalent circumferential ribbon created in CFD is depicted. These ribbons are created at the same radial locations as the experiment and clipped close to the stator wall in line with the probes.

Due to the absence of seed gas in the computational setup, an equivalent formulation using non-dimensional sealing parameter, Φ can be utilized. This is defined in Equation 2.24. Substituting the definition of Φ (see Equations 2.21 and 2.22) with respective subscripts this can be written as,

$$\Phi_o = \frac{\dot{m}_0}{2\pi \rho s \Omega b^2} \qquad \Phi_i = \frac{\dot{m}_i}{2\pi \rho s \Omega b^2} \tag{3.4}$$

where the density is based on the main annulus gas. When this expression is again substituted in Equation 2.24 reduces to,

$$\varepsilon = \frac{\dot{m}_o}{\dot{m}_o + \dot{m}_i} \tag{3.5}$$

Computationally this can be calculated as shown below in Equation 3.6. This is defined in Section 4.3.1 of [12] where it goes by the name mass effectiveness (ε_m) which directly shows how much ingress has entered the cavity using mass fraction.

$$\varepsilon_m = \frac{(m_p)_{local} - (m_p)_{annulus}}{(m_p)_{purge} - (m_p)_{annulus}} \tag{3.6}$$

where,

- $(m_p)_{local}$ refers to purge gas mass fraction at a location of interest
- $(m_p)_{annulus}$ from the outlet of the stage refers to purge gas mass fraction in the annulus
- $(m_p)_{purge}$ refers to purge gas mass fraction at purge inlet

In this work, the variable $(m_p)_{local}$ is measured at a radial ribbon, $(m_p)_{annulus}$ from the stage outlet and $(m_p)_{purge}$ at the purge inlet using absolute mass flow averaging.

3.4 Transient simulation - Monitor points

For the transient simulations, several monitoring points were created throughout the domain. These points are used to monitor the convergence of flow parameters during the simulation. Mass fraction of main annulus gas and static pressure were the main parameters monitored during the simulation. The Figure 3.7 shows the location of the important monitoring points created in the domain.

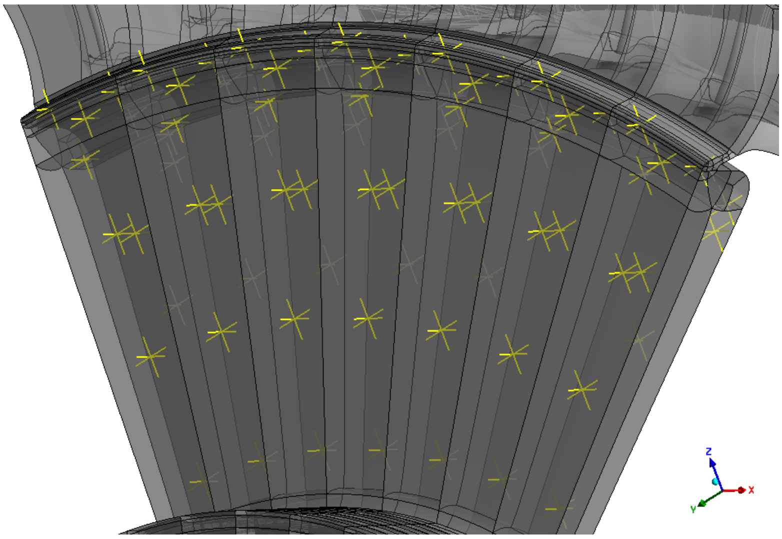

Figure 3.7: Location of monitor points in the domain.

4

Results

In this chapter, a detailed analysis and discussion of the obtained results are presented. The analysis was carried out with increasing modeling complexity and therefore are discussed in the same manner as shown below in Figure 4.1.

Figure 4.1: Result analysis framework.

The non-dimensional parameters relevant to wheelspace cavity analysis were previously defined in Section 2.2.4. Using the initial CFD simulations, these values are re-calculated to compare against experimental data. The Table 4.1 presents these values. Similar to the experiment, the hub radius b used in these calculations are different compared to the actual hub radius [11]. For the sake of consistency and result comparison, this difference is maintained. The density ratio (DR) is calculated on the basis that purge and main annulus flows are at the same reference pressure and temperature .

Parameter	Experiment			CFD		
Re_ϕ	2.77×10^6			3.08×10^6		
Re_{c_x}	9.63×10^5			10.7×10^5		
C_f	0.35			0.35		
C_w	5×10^3	1×10^4	1.5×10^4	5.5×10^3	1.1×10^4	1.7×10^4
Φ_0	0.025	0.050	0.075	0.025	0.050	0.075

Table 4.1: Non-dimensional operating parameters.

Some difference exist between these values due to the ideal gas assumption of the mainstream flow in CFD. However, the most important value, Φ_0, is independent of dynamic viscosity and hence this assumption is justified. The purge-mainstream density ratio DR along with non-dimensional sealing parameter Φ_0, will further be used in this chapter to distinguish between different cases.

4.1 Mesh study

Details of generated meshes were previously provided in Table 3.1. The studies were carried out for the case of DR =1, Φ_0 = 0.050. Further, in order to save computational time, only steady state simulations with SP domain was tested. All the meshes had a $y^+ \leq 5$, lying within the viscous sub-layer. But as seen in the Figure 4.2, a small area near the rim seal exceeded this mark. This is partly due to high velocity at vane exit and a coarse mesh adapted in this region to prevent local divergence experienced during steady simulations.

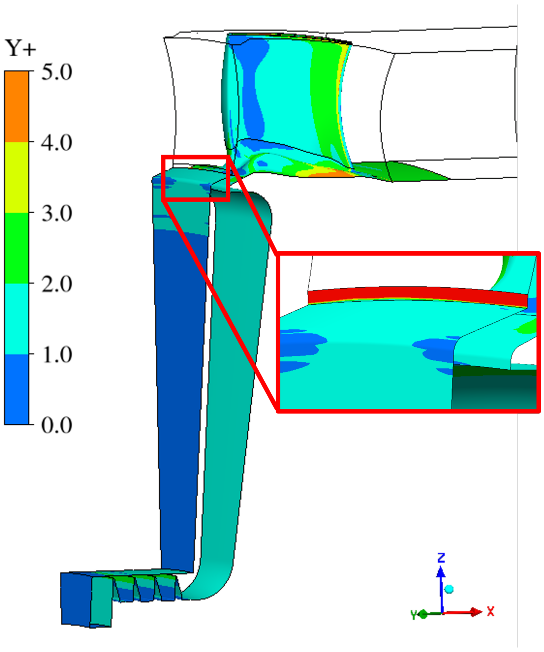

Figure 4.2: Contour plot of wall y^+ for base mesh with high y^+ region enlarged.

Besides y^+, the study involved analyzing total pressure profiles using line probes placed in the rim seal and at blade mid span location as shown in Figure 4.3.

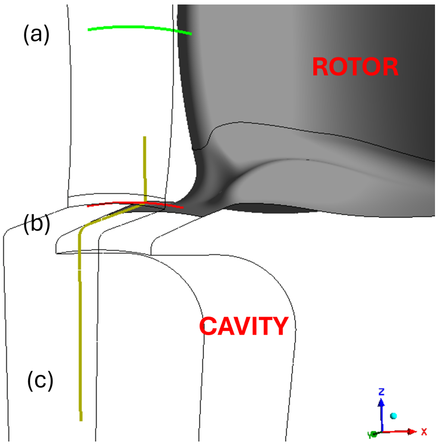

Figure 4.3: Line probe locations

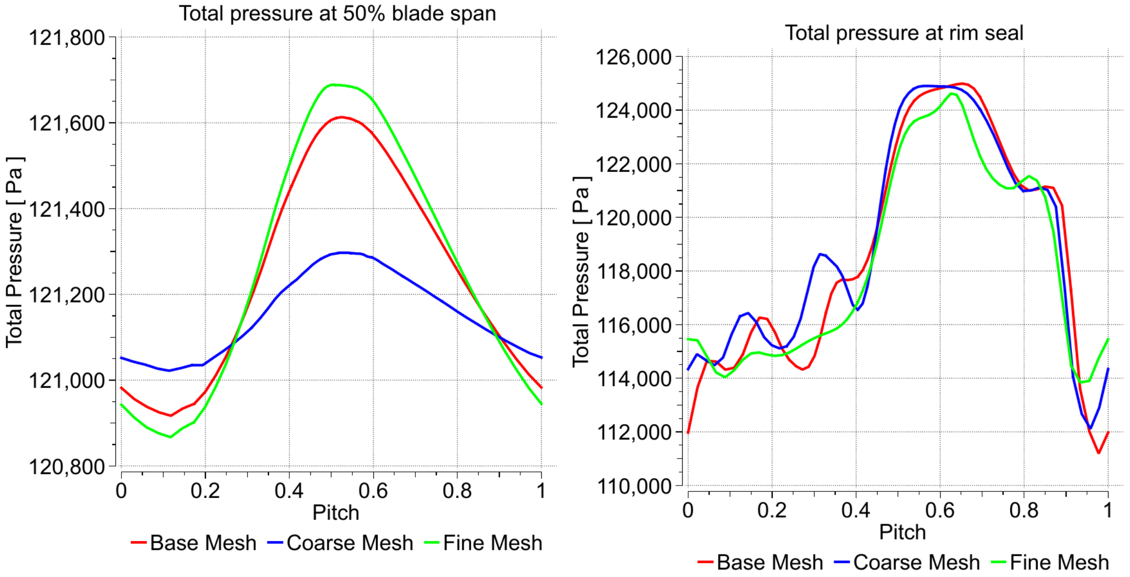

(a) Pitchwise variation at blade mid span

(b) Pitchwise variation at the rim seal

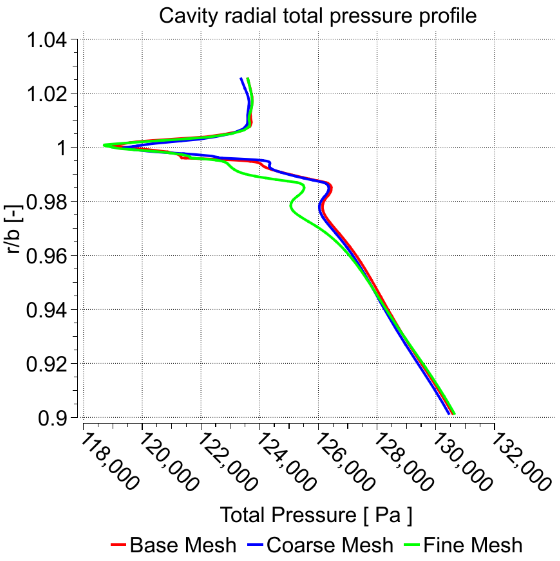

(c) Radial profile through the rimseal

Figure 4.4: XY plot of total pressure profiles at different locations.

The total pressure profile along the aforementioned line probes are portrayed in Figure 4.4 for different meshes. From the Figure 4.4a, a significant difference is observed for the coarse mesh compared to other meshes. However, this huge difference is not observed at the rim seal location shown in Figure 4.4b. Infact, the base and coarse mesh show a similar behavior throughout. The trend for the fine mesh is different at low pitch but manages to follow the trend at high pitch. Again in Figure 4.4c, the radial profile for fine mesh shows a visible difference at about r/b = 0.98. It is observed that base mesh performed satisfactorily in all scenarios and hence was chosen for subsequent simulations.

4.2 Steady state simulations - Single Passage (SP) domain

A total of three simulation cases were performed in this analysis. The non-dimensional reference for these cases are listed in the Table 4.2. About 15000 iterations were required to ensure convergence of flow parameters with RMS residuals in the order of 10^{-5}.

Case description
DR = 1, $\Phi_0 = 0.025$
DR = 1, $\Phi_0 = 0.050$
DR = 1.38, $\Phi_0 = 0.050$

Table 4.2: Steady state simulation cases.

4.2.1 Effect of purge flow rate at constant density ratio

The Figure 4.5 shows for a constant DR = 1, a lower purge of $\Phi = 0.025$ shows significant ingress into the cavity but a complete sealing is observed for the $\Phi_0 = 0.050$. This is because in former the mixing intensity is less due to lower purge level and in-turn the unsteadiness. However this is not case in the latter. Hence, no ingress is observed for the case with steady simulations. Further, as expected with higher purge flow rate, the egress level into main annulus increased.

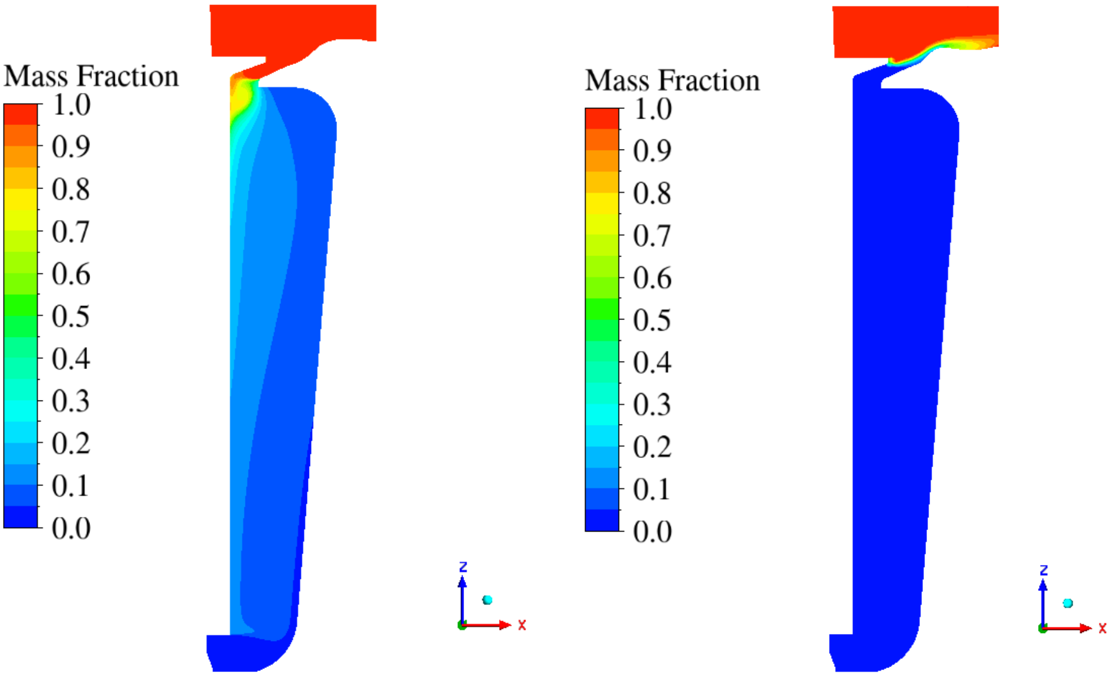

(a) DR = 1, $\Phi_0 = 0.025$ **(b)** DR = 1, $\Phi_0 = 0.050$

Figure 4.5: SP domain - contour plot of hot gas mass fraction in meridional view.

4.2.2 Effect of density ratio at constant purge flow $\Phi_0 = 0.050$

The Figure 4.6 show the mass fraction contour for same purge flow of $\Phi_0 = 0.050$ but different density ratios (DR =1, 1.38). Again no ingestion activity is observed for these cases as expected. But between the two purge gases no discernible difference were also seen. This suggests an insensitivity to density effects with SP domains.

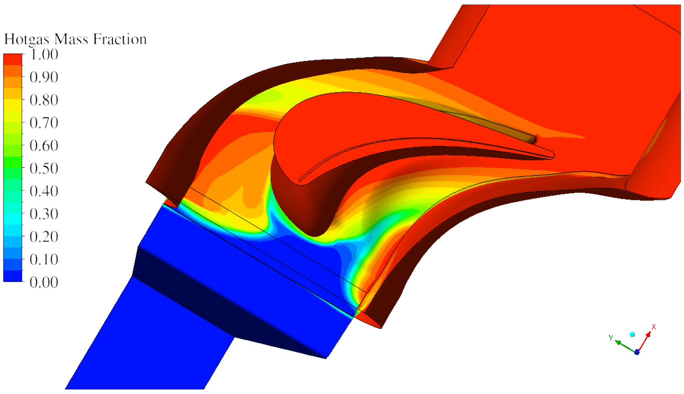

(a) DR = 1, $\Phi_0 = 0.050$

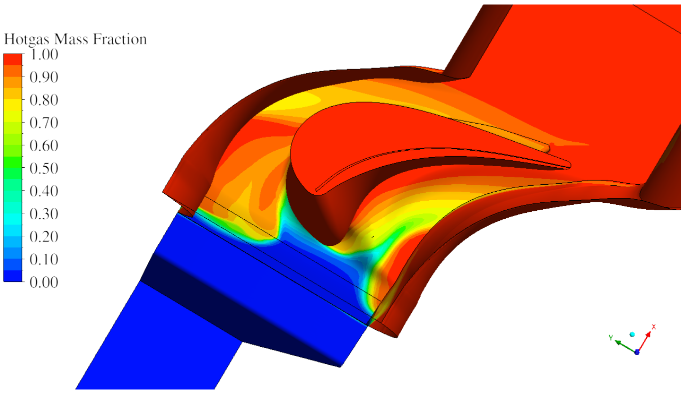

(b) DR = 1.38, $\Phi_0 = 0.050$

Figure 4.6: SP domain - contour plot of hot gas mass fraction from isometric top-down point of view.

4.2.3 Comparison of sealing effectiveness

Experimental data show that for the cases tested above there exists significant hot gas ingestion activity in the cavity. However, as seen above this is not captured with a sealing flow rate $\Phi_0 = 0.050$ while some ingress activity is observed in $\Phi_0 = 0.025$. A comparison of sealing effectiveness between experiment and CFD is shown below in Figure 4.7 for all three cases. Clearly, a significant under prediction of ingress or in other words, over-prediction of sealing effectiveness is observed with CFD estimations. Notably, for the case DR =1, $\Phi_0 = 0.025$ represented by Figure 4.7a, a good agreement exists at r/b =0.98 but for other radial locations CFD still over predicts sealing effectiveness.

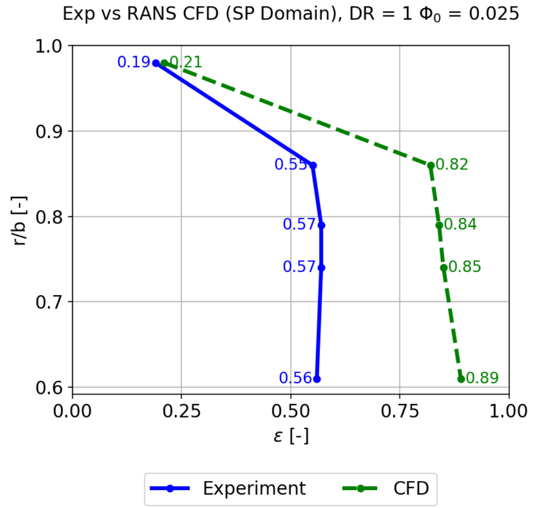

(a) DR = 1, $\Phi_0 = 0.025$

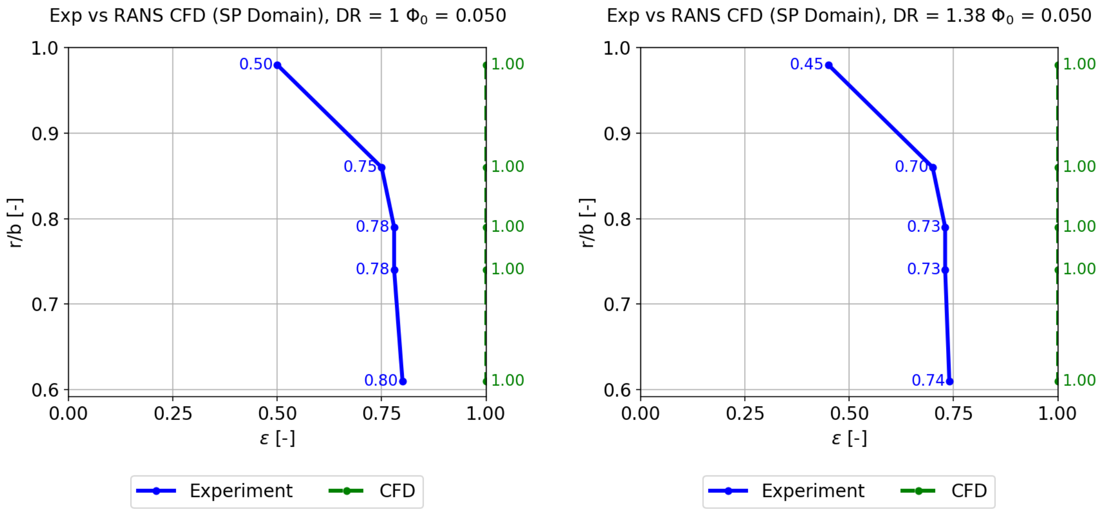

(b) DR = 1, $\Phi_0 = 0.050$.

(c) DR = 1.38, $\Phi_0 = 0.050$

Figure 4.7: SP Domain - Comparison of sealing effectiveness experiment vs steady CFD.

4.3 Steady state simulations - Sector domain

Using the SP domain results, the sector domain simulations were initialized. The cases tested here are the same as preceding section which is tabulated in Table 4.2. About 10000 to 15000 iterations were required for flow convergence with RMS residuals reaching 10^{-4} before oscillating about a mean value.

4.3.1 Evaluation of density effects - Sector domain

The Figure 4.8 depicts contour plot of hot gas distribution in a Sector domain for varied density ratio. While the single passage domain showed an insensitivity to purge gas density, sector domain shows some visible differences. Comparing both contours, it is evident that with high DR of 1.38, a higher area of egress observed behind the rotor blade. This is indicated by a hot gas mass fraction value < 1.

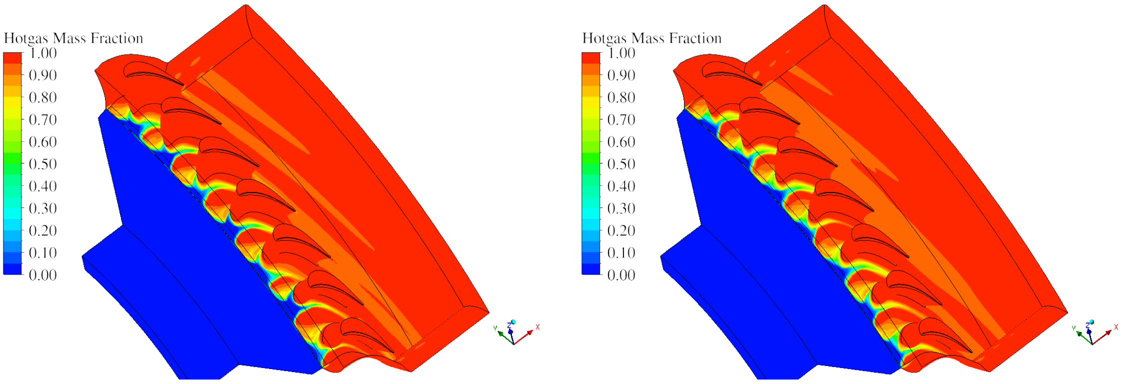

(a) DR $= 1$, $\Phi_0 = 0.050$ **(b)** DR $= 1.38$, $\Phi_0 = 0.050$

Figure 4.8: Sector domain - contour plot of hot gas mass fraction in isometric top-down point of view.

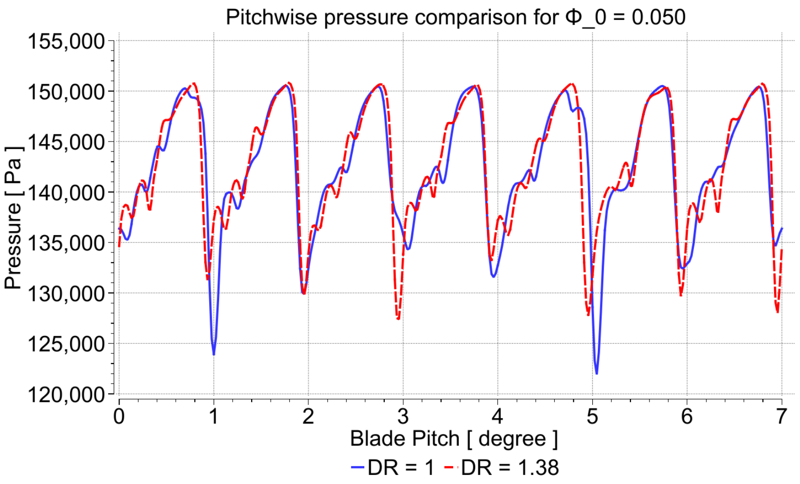

Figure 4.9: Sector domain - pitchwise variation of static pressure at blade rim seal for $\Phi = 0.050$.

Since no ingress was observed in these cases (DR $=1$ $\Phi_0 = 0.050$ and DR $= 1.38$ $\Phi_0 = 0.050$), the comparison is made through tangential pressure distribution across blade pitches. The Figure 4.9 showcase the same where the difference can be observed clearly. The peak between the two purge gases largely remain the same but the crest for the former reach lower values than the latter. Further, a slight in the crest location for blade pitch 5 is also observed for the DR $= 1$. Therefore, a high density gas could provide better sealing as the pressure differential is lower. However, since no the cavity ingress is not captured, this inference cannot be made with steady state simulations which is to be expected.

4.3.2 Comparison between SP and Sector domain

The SP model assume repeating patterns between blade pitches due to the periodic boundary conditions. However, the Figure 4.9 shows that for a purge gas, the variation between adjacent blades are not repetitive. Hence modeling ingress using single passage domain can lead to under prediction of ingress. To support this, Figure 4.10 depicting tangential variation of hot gas mass fraction for both domains are plotted at the rim seal location. The SP domain is instantiated multiple times for a better visualization.

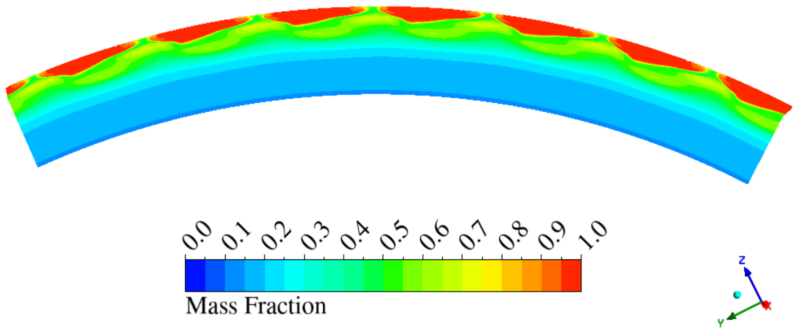

(a) SP domain (replicated to match the sector domain).

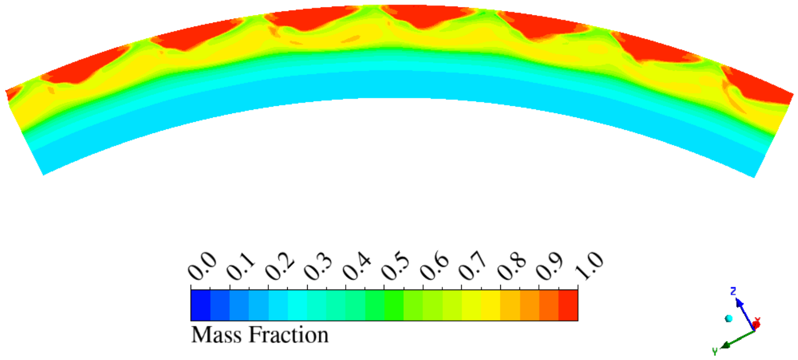

(b) Sector domain

Figure 4.10: Comparison of hot gas mass fraction, SP vs Sector domain for DR $= 1$ $\Phi_0 = 0.025$ (contour plot with 21 levels).

As seen in the contour, the ingress levels are different for the two. Some disturbance exist in the middle and right side of Figure 4.10b which are not observed in Figure 4.10a. More importantly a higher ingress (region in yellow, mass fraction = 0.8) is observed in former but with SP domain a lower ingress is observed (region in green, mass fraction = 0.5). In terms of sealing effectiveness, plotted in Figure 4.11 although far from experimental value, a relatively closer match is achieved with sector domain.

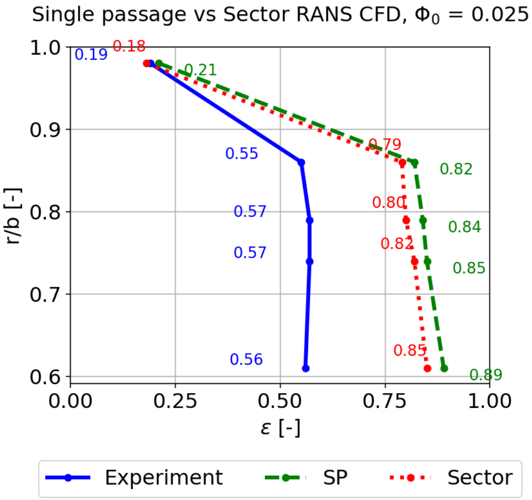

Figure 4.11: Comparison of sealing effectiveness for DR =1, $\Phi_0 = 0.025$. Experiment vs SP domain vs Sector domain.

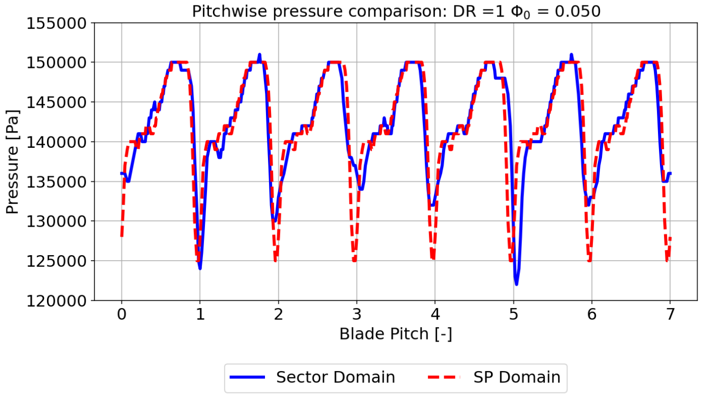

(a) DR = 1, $\Phi_0 = 0.050$

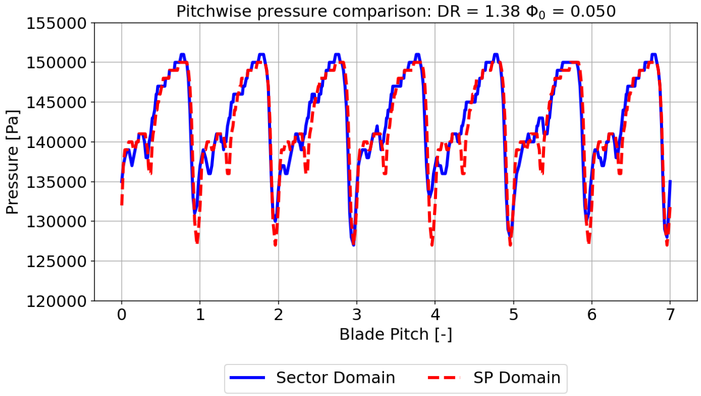

(b) DR = 1.38, $\Phi_0 = 0.050$

Figure 4.12: Comparison of pitchwise pressure variation, SP vs Sector domain.

For the cases, DR = 1, $\Phi_0 = 0.050$ and DR = 1.38, $\Phi_0 = 0.050$ the difference between single passage and sector domain are shown in Figure 4.12 in terms of static pressure variation at the rimseal location. The reason for choosing pressure is same as before. Here as well, the tangential variation is dissimilar between the single passage and sector domain.

To summarize, the two part steady state analysis has shown that, they severely under predict or cannot capture the wheelspace cavity ingress at all. Further, sector models should be preferred due to the enforced periodicity in single passage domains.

4.4 URANS simulations

As the next step in the analysis, URANS simulations were performed using the sector domain. These simulations are initialized from steady state sector domain solutions. In total, six cases at design point tested in the experiments, were simulated and their corresponding non-dimensional reference is tabulated in Table 4.3. The RMS residuals were in the order of 10^{-8}. All cases were simulated for a minimum of 2 flowthroughs or 1 revolution with some cases requiring upto 3 revolutions to reach a statistical steady state. Post which an averaging run was carried out for 1 flowthrough or half a revolution. Each revolution took about a week time under 600 core power with averaging runs costing even more.

Case Description
DR = 1, $\Phi_0 = 0.075$
DR = 1, $\Phi_0 = 0.050$
DR = 1, $\Phi_0 = 0.025$
DR = 1.38, $\Phi_0 = 0.075$
DR = 1.38, $\Phi_0 = 0.050$
DR = 1.38, $\Phi_0 = 0.025$

Table 4.3: URANS simulation cases.

The Figure 4.13 depicts the CFL number in the cavity for the highest convection rate case, DR =1 $\Phi_0 = 0.075$. A CFL ≤ 2 was achieved in the wheelspace for the calculated timestep of 2.32×10^{-6}s.

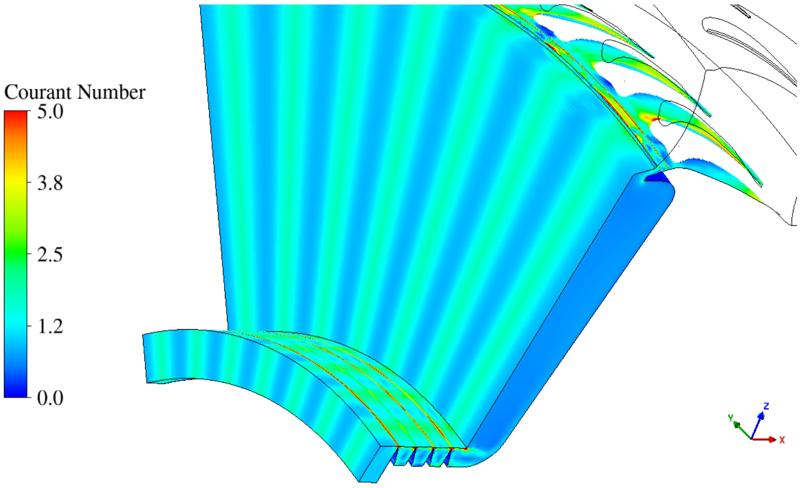

Figure 4.13: Isovolume of cavity with CFL ≤ 5 limiter for DR =1, Φ_0 =0.075.

This section is further divided into three based on non-dimensional sealing parameter Φ_o with each section comparing the two density ratio DR = 1, 1.38. The time-averaged results are presented in meridional view, cut at the middle of the sector, and in tangential perspective. For each sub-section the CFD are results are examined against experimental sealing effectiveness.

4.4.1 Comparison between DR = 1 and DR = 1.38 for $\Phi_0 = 0.075$

The DR =1, $\Phi_0 = 0.075$ case was run for a total of ≈ 2.5 revolutions. As observed from the Figure 4.14, only a small amount of ingress has penetrated the cavity and no circumferential variation is observed close to the stator wall. This level of ingress is expected as a higher amount of purge provides better sealing at the cost of performance.

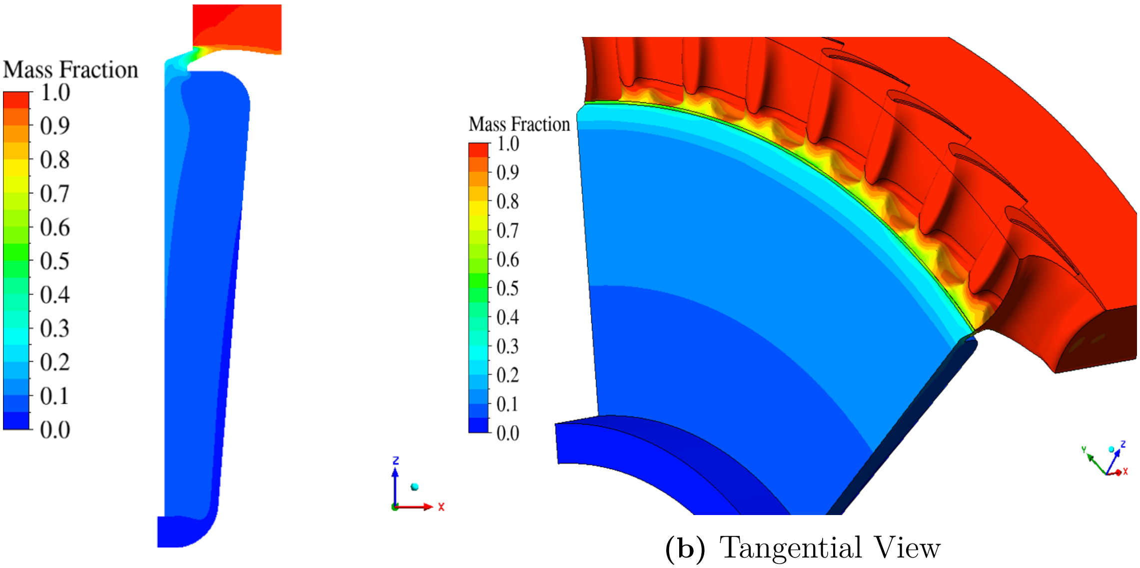

(a) Meridional view

(b) Tangential View

Figure 4.14: Time averaged hot gas mass fraction for DR = 1.

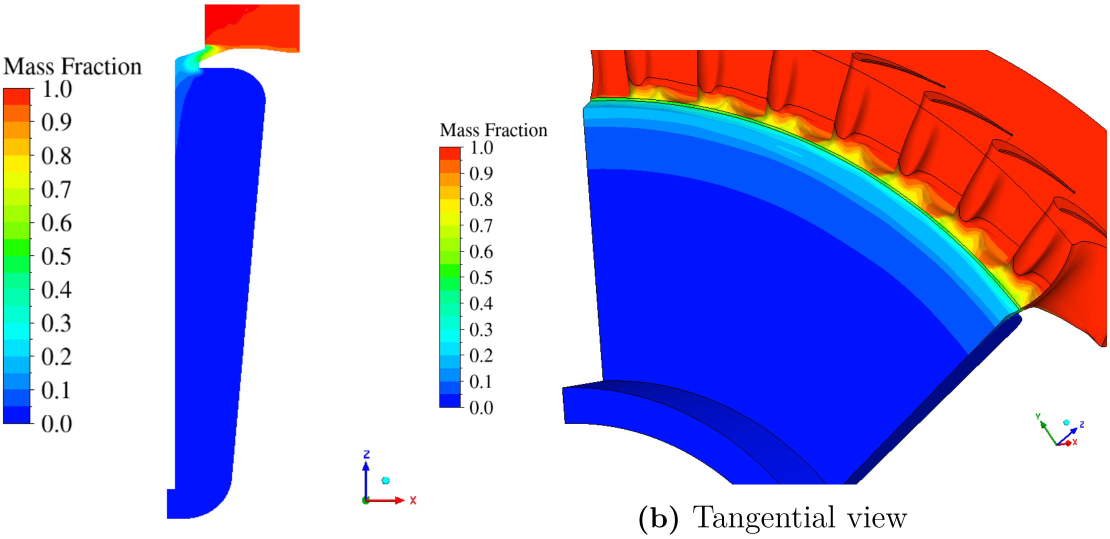

(b) Tangential view

(a) Meridional view

Figure 4.15: Time averaged hot gas mass fraction for DR = 1.38

In case of argon DR =1.38 shown in Figure 4.15, a significant sealing has been observed. No visible ingress was seen past the non-dimensional radius r/b = 0.98. And again tangentially, no difference between blade passages are observed. Due to almost complete sealing, this case required only about ≈ 1.5 revolutions, excluding averaging, to reach a statistical steady state.

The sealing effectiveness was calculated along the ribbons spanning tangentially as described in Section 3.3. The time and circumferentially averaged sealing effectiveness for the two cases are shown in Figure 4.16. Almost accurate predictions were observed for DR =1 in Figure 4.16a. At r/b =0.98, a significant difference exists. The reason behind this could be the high amplitude periodic fluctuations observed at this location during the simulation.

In case of DR = 1.38 shown in Figure 4.16b, at all locations deviation from experimental values are significantly higher. Further, the denoted values shows better sealing than DR = 1 shown in Figure 4.16a.

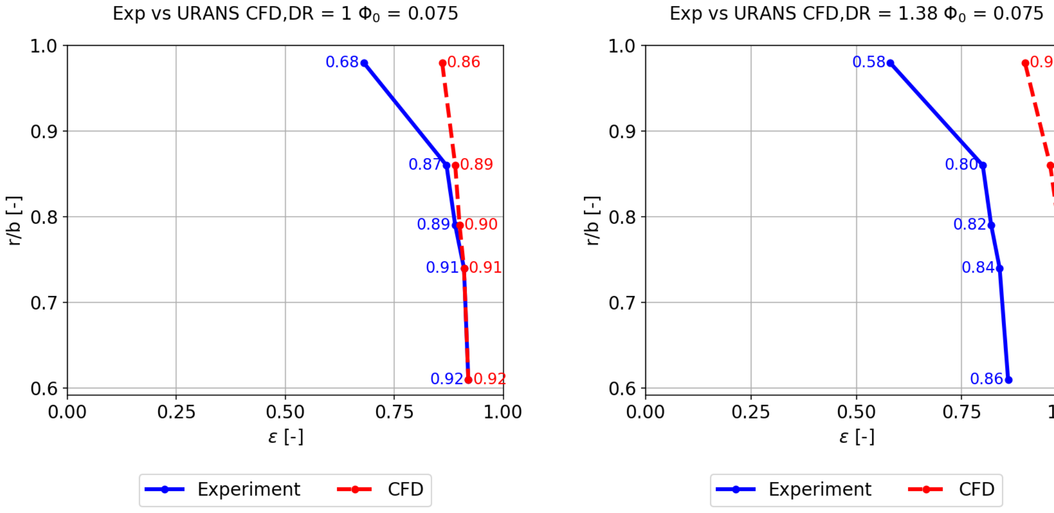

(a) DR = 1 **(b)** DR = 1.38

Figure 4.16: Time and circumferential averaged sealing effectiveness comparison experiment vs CFD for $\Phi_0 = 0.075$.

4.4.2 Comparison between DR = 1 and DR = 1.38 for $\Phi_0 = 0.050$

With reduction in purge, the hot gas ingestion has increased in the cavity. As observed in Figure 4.17a , more hot gas ingress into the cavity. Further, a part of ingress also moves to the rotor disc through the inviscid core. This is observed at the highest and lowest radial extremes. A total ≈ 2 revolutions were required to reach a stable point. Further, no tangential variation is observed.

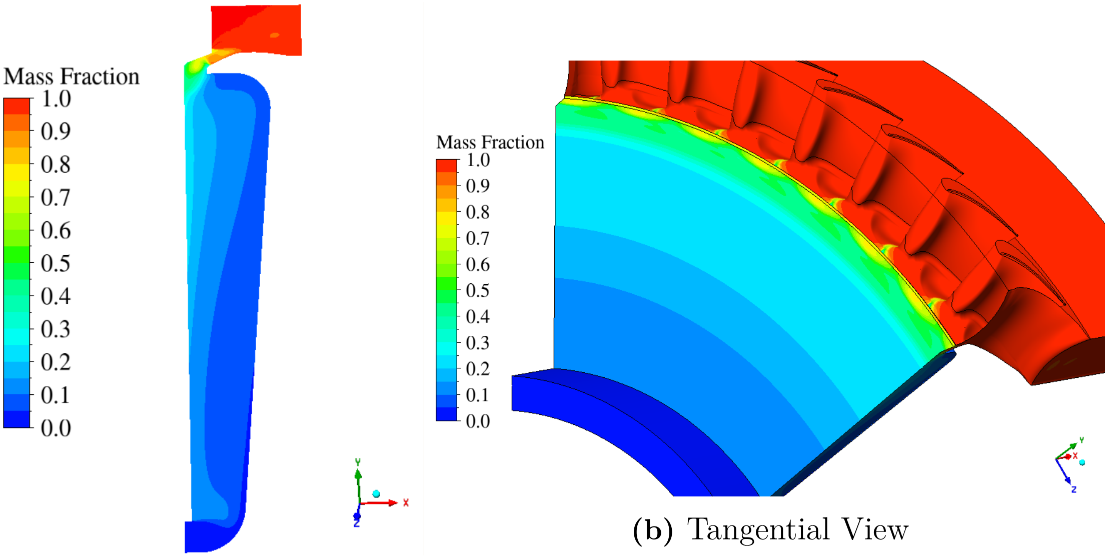

(a) Meridional view

(b) Tangential View

Figure 4.17: Time averaged hot gas mass fraction for DR = 1.

The Figure 4.18 shows the corresponding high density purge flow behavior. These simulations were run for a total of ≈ 3 revolutions. Again compared to DR =1 in Figure 4.17, a lower overall ingress is seen. On closer look at the rim seal, a greater area in green, showing high ingress is observed. This is clearly visible in the tangential view shown in Figure 4.18b where a rotating high ingress region could be observed. Similar to the case DR =1, $\Phi_0 = 0.075$ high amplitude periodic fluctuations were observed in the case and is surmised to be the reason behind this.

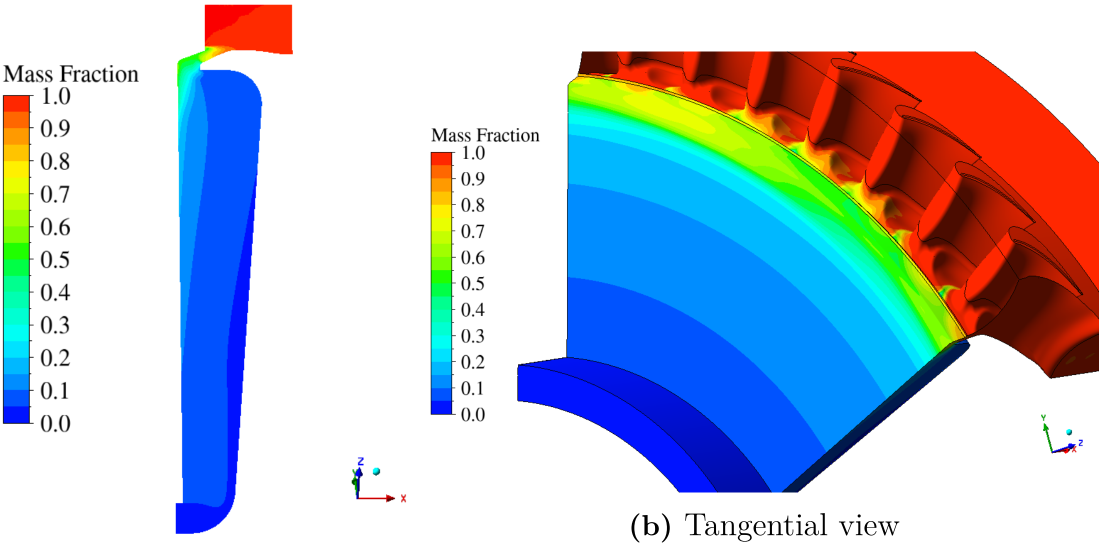

(a) Meridional view

(b) Tangential view

Figure 4.18: Time averaged hot gas mass fraction for DR = 1.38

Comparing the radial sealing effectiveness values with experiment, a good overall agreement is observed for DR =1. Yet again for DR =1.38, the CFD predictions are significantly higher than experiments and DR =1. The highest radial point r/b = 0.98, ε =0.46 is one point that deviates due to the local high in mass fraction observed before.

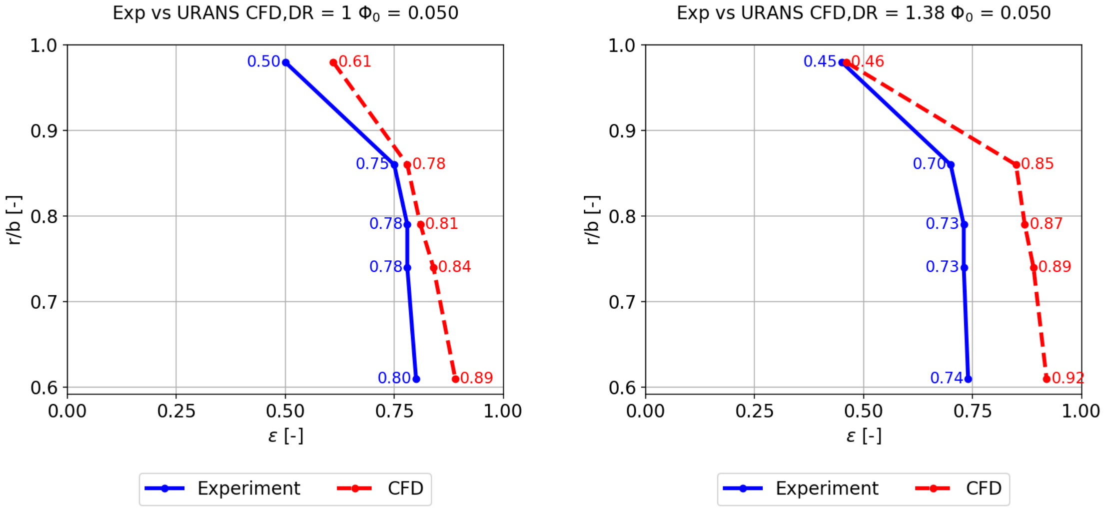

(a) DR = 1 **(b)** DR = 1.38

Figure 4.19: Time and circumferential averaged sealing effectiveness comparison experiment vs CFD for $\Phi_0 = 0.050$.

4.4.3 Comparison between DR = 1 and DR = 1.38 for $\Phi_0 = 0.025$

The lowest purge cases were ran for the least amount of time with DR =1 for ≈ 1 and DR =1.38 for ≈ 1.5 revolutions as they quickly reach a statistical steady state. In both cases no tangential difference in ingress levels were observed between adjacent blade passage. Similar to previous cases, a reduced level of ingress was observed with the high density DR =1.38 purge gas.

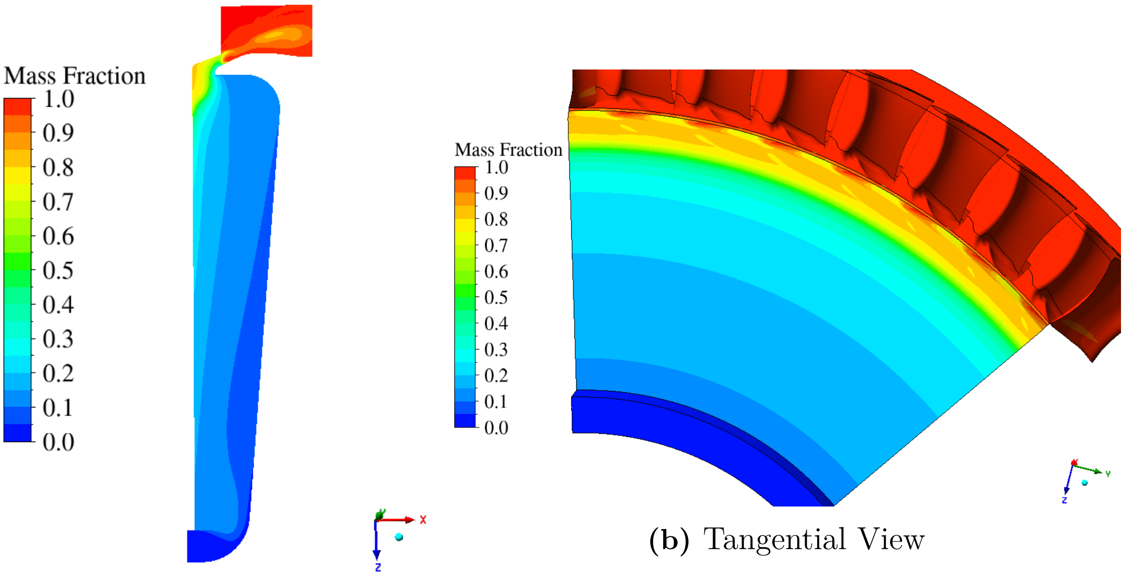

(a) Meridional view

(b) Tangential View

Figure 4.20: Time averaged hot gas mass fraction for DR = 1.

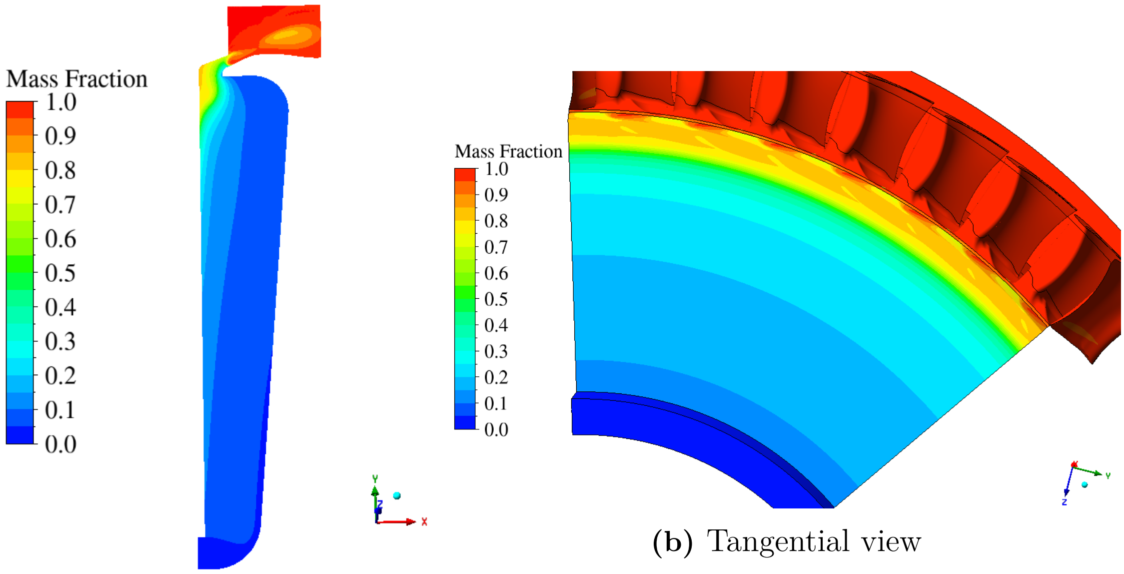

(a) Meridional view

(b) Tangential view

Figure 4.21: Time averaged hot gas mass fraction for DR = 1.38

Although the other cases showed a good agreement with experimental data, for the low purge cases the CFD estimations showed a significant 40% error in sealing effectiveness as seen in Figure 4.22a. Only the highest radial location agreed well with the experimental data. But similar to other purge cases a high density DR = 1.38 purge gas showed a better sealing than low density purge gas DR =1.

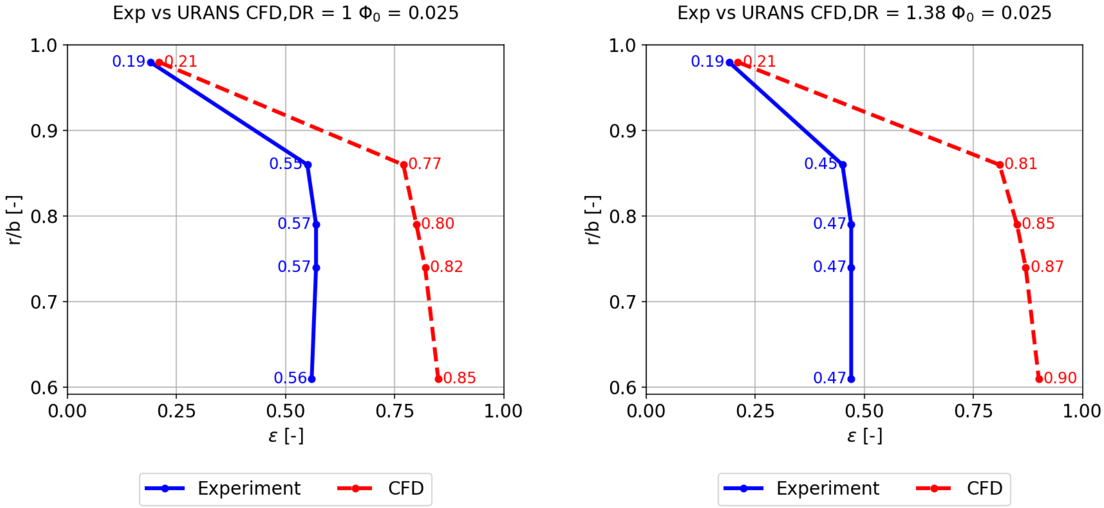

(a) DR = 1 **(b)** DR = 1.38

Figure 4.22: Time and circumferential averaged sealing effectiveness comparison experiment vs CFD for $\Phi_0 = 0.025$.

4.5 Effect of purge-mainstream density

From the comparison of results between experiment and CFD, it is evident for DR =1, CFD predictions show a satisfactory agreement. While for DR = 1.38 CFD predictions show higher difference. Further for DR = 1.38, the sealing effectiveness is consistently higher than the former. This contradict the conclusion made by the experimental study, where DR=1.38 showed a lower sealing than DR =1 [11]. For ease of comparison, both experiment and CFD results are consolidated in the figure 4.23.

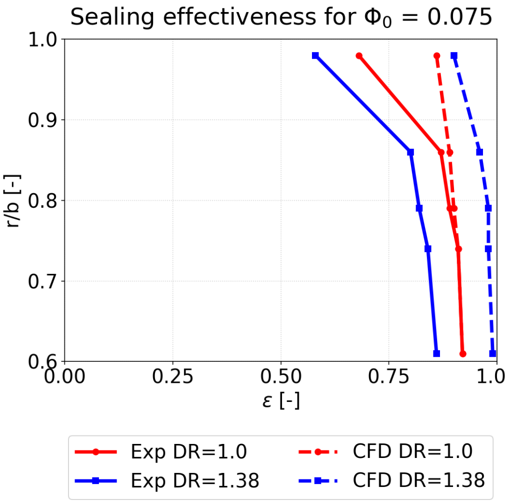

(a) $\Phi_0 = 0.075$

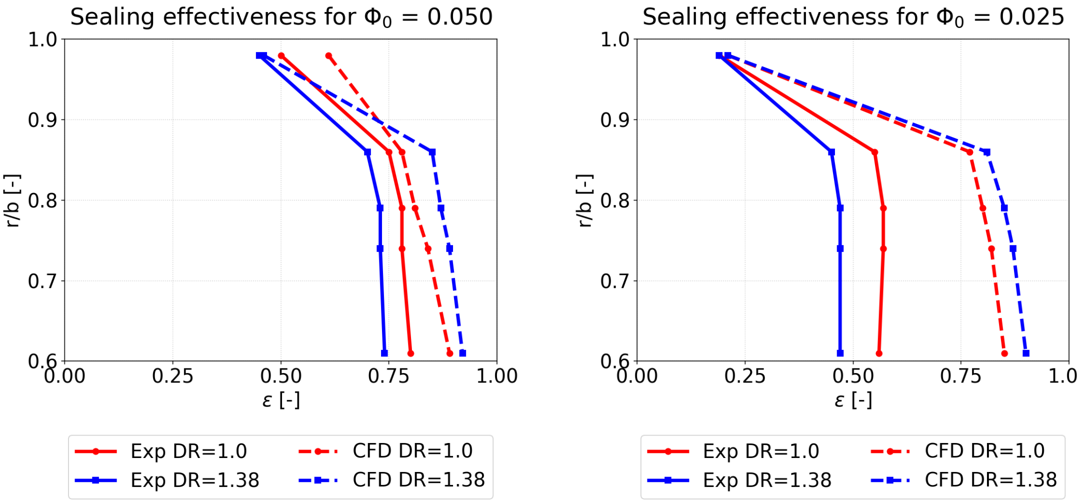

(b) $\Phi_0 = 0.050$.

(c) $\Phi_0 = 0.025$

Figure 4.23: Time and circumferential averaged sealing effectiveness comparison experiment vs CFD consolidated. Adopted from [11].

To explain this contradiction, it is important to note the seed gas concentration level used in the experiment. To reiterate, sealing effectiveness was estimated in the experimental study by introducing non-reacting seed gas along with purge flow. The seed gas used in the study was CO_2, introduced at a concentration level of 1%. On the other hand, CFD model did not use seed gas but rather utilized the mass fraction to evaluate sealing using Equation 3.6 .

In the work by D. Graikos [12], a similar experimental study was conducted with data collected at 1% concentration of CO_2. With same concentration level, CFD study was also performed showing a good agreement. However, when the CFD model was simulated with 100% concentration of CO_2 creating a DR= 1.65, a higher sealing effectiveness was observed. This difference is represented by Figure 4.24 where the difference in sealing between a 1% CO_2 concentration (in blue) to 100% CO_2 concentration (in red) is clear. With this finding they conclude the discussion by sharing that increasing the DR lead to better sealing and experimental data collected at low concentration of seed gas overestimate ingress. This discussion can be found in Section 4.3.1 of the work [12].

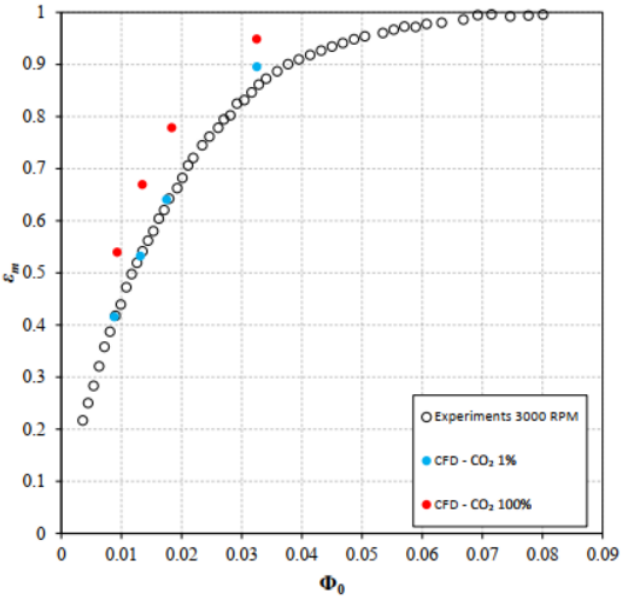

Figure 4.24: Sealing effectiveness vs Φ_o curve. Experimental and computational data. Open circles - experiment, blue - CFD with 1% purge CO_2 seeding and red - CFD with 100% purge CO_2 seeding [12].

While this finding can explain the deviation observed in DR =1.38 for $\Phi_0 = 0.075, 0.050$ purge flow rates, the low purge case $\Phi_0 = 0.025$ despite these effects show a significant deviation. This is due to the slow convection rate associated with low purge flow rates and hence requires a longer runtime to observe the full ingress effect.

4.6 SBES simulations

4.6.1 Comparison of URANS vs SBES

In an effort to validate one of the low purge cases, DR =1, $\Phi_0 = 0.025$, was simulated for a longer period of 3 revolutions using URANS. Additionally, SBES simulation was also performed to study the influence of turbulence modeling. Due to time constraints, only one of the cases could be carried out and to decide a victor an instantaneous comparison was made at the same point in time.

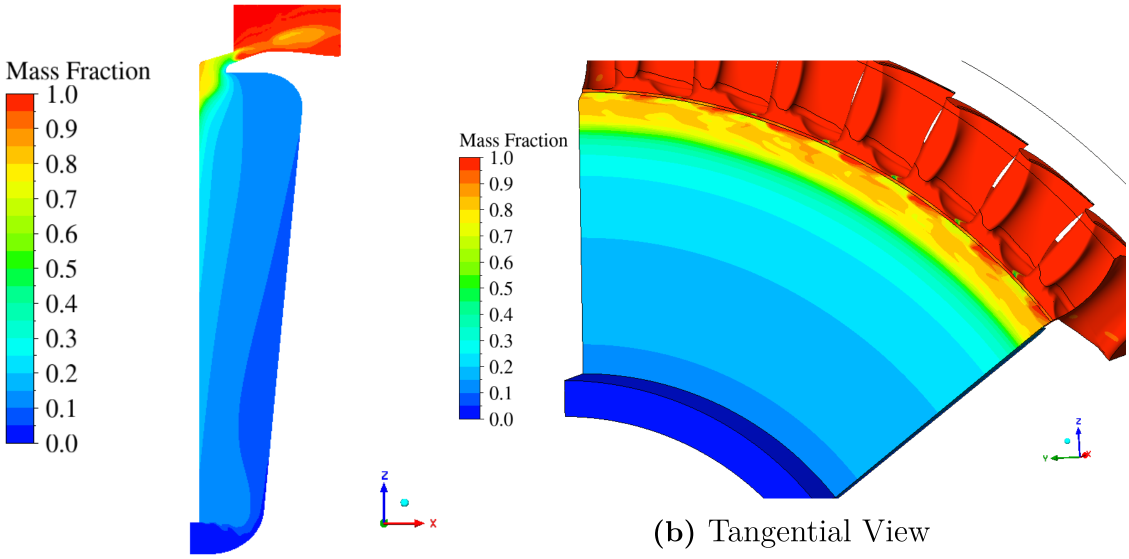

(b) Tangential View

(a) Meridional view

Figure 4.25: Instantaneous hot gas mass fraction with URANS at 3 revolutions.

The Figure 4.25 shows the instantaneous URANS data after 3 revolutions. It was observed that no significant improvements in ingress were seen compared to the averaged data shown before in Figure 4.20. However for SBES shown in Figure 4.26 some differences especially at the high radial points were observed. And in tangential direction (Figure 4.26b) a higher ingress is evident than the URANS counterpart (Figure 4.25b). It can be argued that this difference is created due to amount of turbulence being resolved in SBES is more than the URANS.

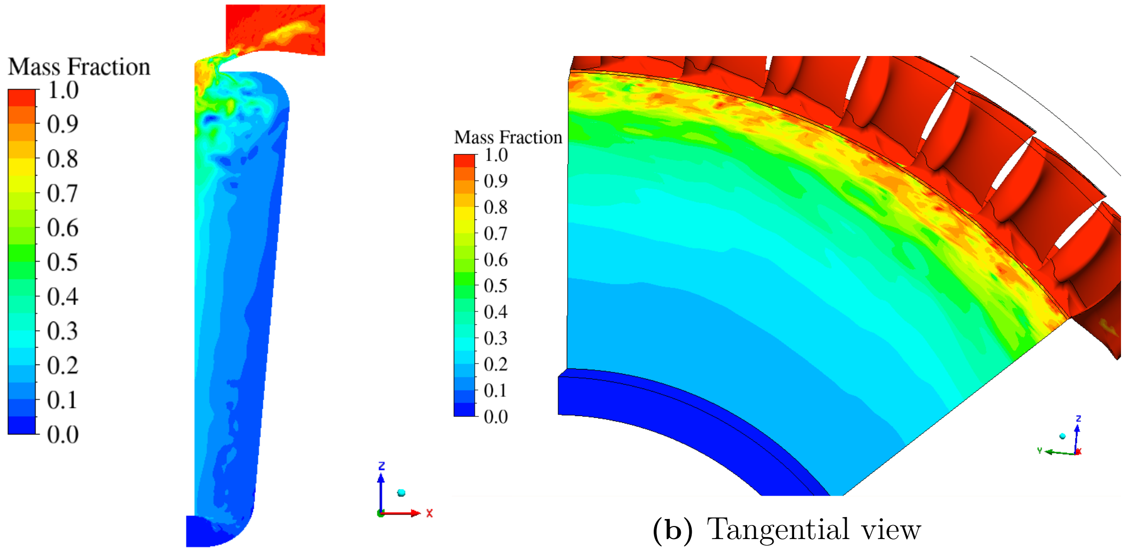

(b) Tangential view

(a) Meridional view

Figure 4.26: Instantaneous hot gas mass fraction with SBES at 3 revolutions.

Further, the sealing effectiveness at this time instant was also compared between the two models and plotted in Figure 4.27. As expected, for the non-dimensional radial points located between 0.7 to 0.9 SBES has predicted a lower sealing effectiveness closing in on the experimental data. But as this is an instantaneous comparison the experimental data is not shown here. Based on these observations, it was decided to simulate the low purge case using SBES.

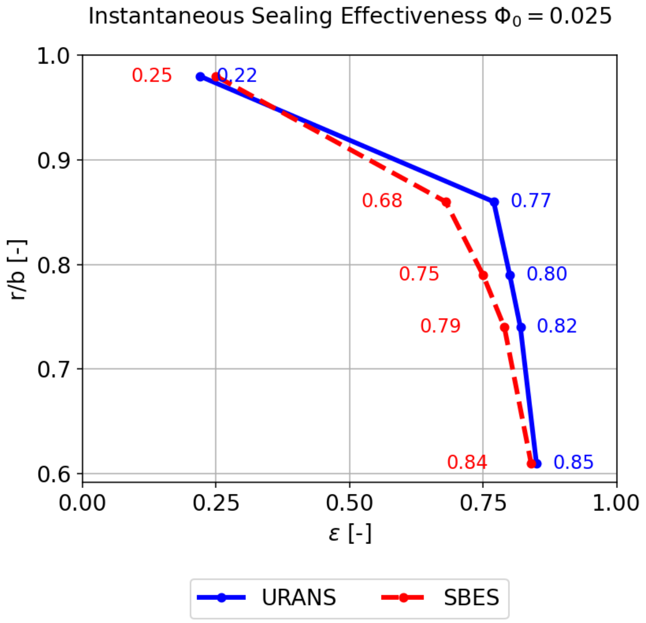

Figure 4.27: Circumferentially averaged sealing effectiveness comparison at a time instant. URANS vs SBES.

4.6.2 Time averaged results

The SBES simulations were run for a total of 7 revolutions post which an averaging run was carried out for half a revolution. With SBES, the RMS residuals were in the order of 10^{-4}. This is expected as the instantaneous turbulence are being resolved. The computational cost was notably high when using SBES, requiring a total of 9 weeks, with 2 weeks dedicated solely to the averaging run.

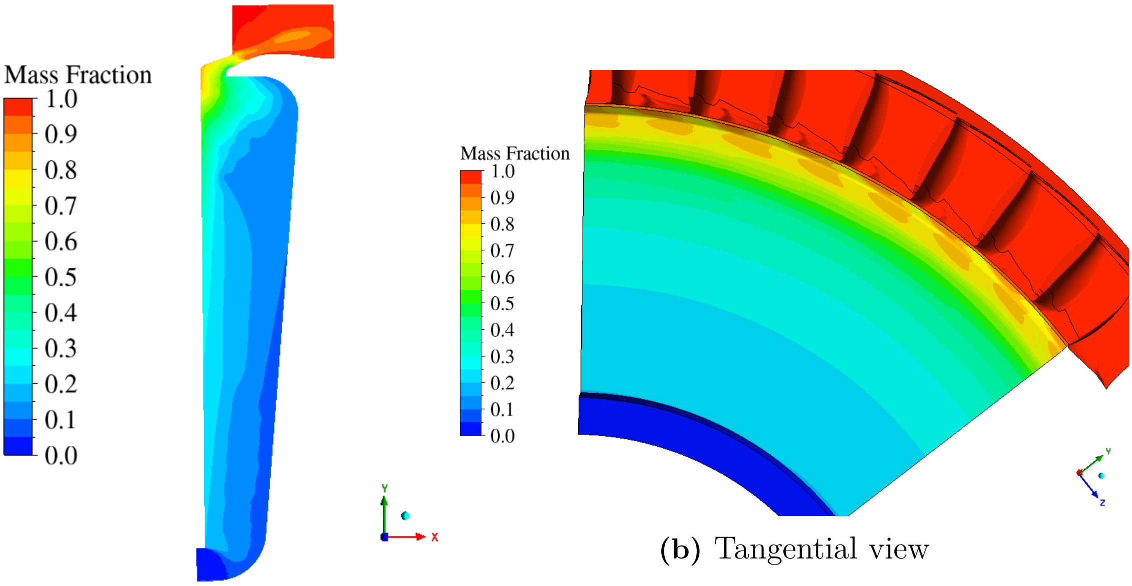

(b) Tangential view

(a) Meridional view

Figure 4.28: Time averaged hot gas mass fraction for DR = 1, Φ_o =0.025 using SBES.

As observed from the figure 4.28, with longer using SBES, the levels of ingress has improved significantly. Similar to all the preceeding cases, no circumferential variation at the stator wall.

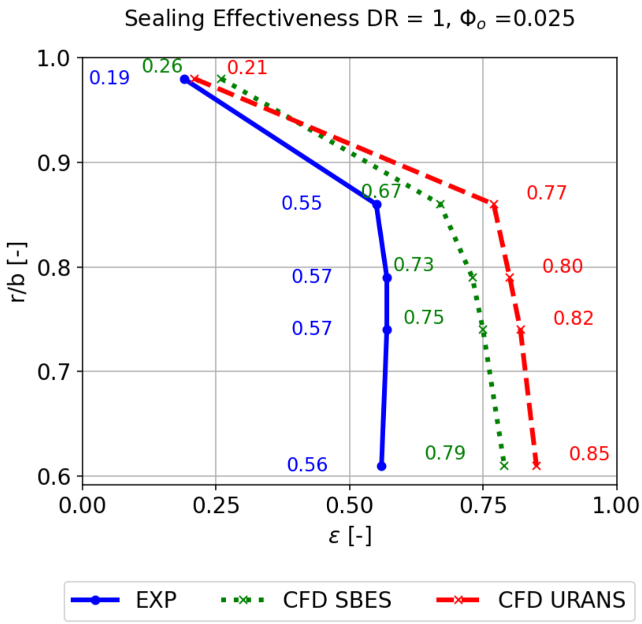

Figure 4.29: Time and circumferentially sealing effectiveness comparison for DR =1 Φ_o =0.025.

On comparing the sealing effectiveness, it is evident that running the simulation longer has reduced the error margin. Therefore, it is safe to conclude that the low purge cases requires more revolutions to be simulated. This conclusion also falls in line with the work [25], where it has been recorded that low purge cases required >30 revolutions equating to of $60,000$ core hours for a 30° sector model.

5

Conclusion

Performance of industrial gas turbines depends on Turbine Inlet Temperature (TET) from thermodynamic cycle point of view. However, not all areas of the turbine are designed to protect the blade. Among such areas lies the rotor-stator wheelspace cavity prone to hot gas ingestion which is traditionally cooled using pressurized air bled from a suitable compressor stage. This is known as *Purge cooling*. Traditional experimental rigs work under cold flow conditions and hence is not representative of real engine conditions where temperatures reach 1700°C. Therefore, the effect of difference in density between purge and mainstream gases are often neglected.

This thesis investigated the effect of this density difference or Density Ratio (DR) by means of CFD simulations. Results of prior experimental studies conducted at KTH University [11] were used to validate the CFD predictions. Air (DR =1) and Argon (DR =1.38) were the purge gases tested at design point RPM of 10540 (C_f = 0.35) for three non-dimensional purge flow rates $\Phi_o = 0.025, 0.050, 0.075$. The study involved a gradual increase of simulation complexity starting from steady state to URANS and further hybrid RANS-LES model - SBES for the lowest purge case, $\Phi_o = 0.025$. The ingress is quantified using the non-dimensional parameter, Sealing effectiveness.

Key findings

Steady state simulations

Steady state simulations were found to be inadequate for accurately predicting hot gas ingestion phenomena. An exception was observed for the lowest purge rate of $\Phi_o = 0.025$, where hot gas ingestion occurred due to low mixing intensity associated with the minimal purge flow. However, the level of ingestion was under-predicted. Additionally, the use of sector domains representing approximately 51° of the full 360° annulus revealed that ingress is further suppressed by the enforced periodicity associated with single-passage domains.

URANS simulations

URANS simulations were conducted for all six cases (DR = 1, 1.38; $\Phi_o = 0.025$, 0.050, 0.075). As expected, an increase in purge flow rate led to higher sealing effectiveness across all cases. However, when comparing different purge gases at the same purge flow rate, the heavier purge gas (Argon, DR = 1.38) demonstrated better sealing effectiveness than the lighter purge gas (Air, DR = 1), which contradicted experimental findings. Further analysis revealed that the concentration of seed gas plays a critical role in ingress estimation. Lower seed gas concentrations lead to overestimation of ingress, while 100% seed gas concentration demonstrated higher sealing effectiveness, as detailed in Section 4.3.1 of [12]. This suggests that heavier purge gases may offer superior ingress prevention.

Low purge cases

Among all cases, the low purge rate ($\Phi_o = 0.025$) cases exhibited the poorest agreement with experimental results. This discrepancy is attributed to the slower convection rate associated with low purge levels, which requires longer simulation runtimes to capture the full extent of the phenomena. To address this, an extended simulation run using the SBES model was conducted for 7 rotor revolutions. Although this showed some improvement, it is evident that low purge rate simulations require substantial revolutions for accurate ingress prediction.

5.1 Recommendations for future work

The findings of this study have highlighted several promising avenues for future research on this topic. In particular, those that can be immediately pursued in future research work are recommended from experimental and computational perspectives.

Experimentally, it is worthwhile to run test campaigns using 100% seed gas concentration to re-evaluate the impact of density ratio on cavity sealing.

Computationally, the immediate recommendation is to simulate for a higher revolution count, especially for low purge cases. Additionally, investigating off-design cases where combined ingress effects occur presents another promising avenue for research. However, as evident from this study, the associated computational time and cost are high for industrial-scale simulations. Therefore, it is important to consider reduction in domain size which could be done in two ways:

1. The Transient Blade-Row (TBR) with profile transformation model in Ansys CFX can minimize the number of simulated passages
2. Based on the various literature reviewed the main annulus can be simplified as shown below in Figure 5.1 to focus on the cavity.

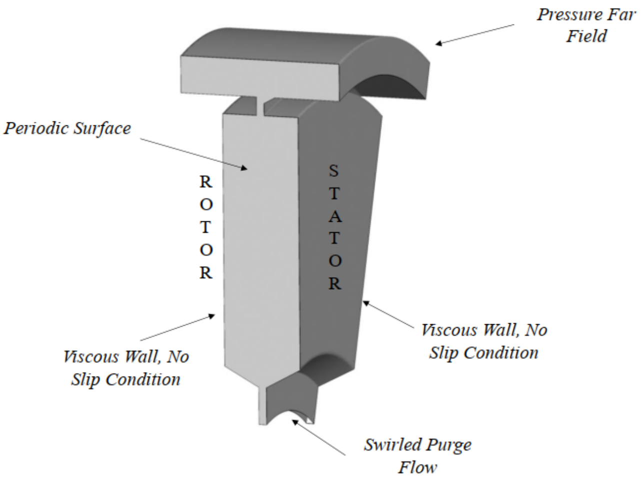

Figure 5.1: Computational domain utilized in [12].

Bibliography

[1] J. Dahlqvist, *Cavity Purge Flows in High Pressure Turbines.* PhD thesis, KTH Royal Institute of Technology, 2017. https://urn.kb.se/resolve?urn=urn:nbn:se:kth:diva-218468.

[2] KTH Royal Institute of Technology, "Test Turbine." `https://www.kth.se/en/eecs/test-turbines-1.890675`, 2024.

[3] R. Lewis, *Turbomachinery Performance Analysis.* Butterworth-Heinemann, 1996. ISBN: 9780080543321 https://books.google.se/books?id=kmaJl-WmwJkC.

[4] R. Royce, *The Jet Engine.* Wiley, 2015. ISBN: 9781119065999 https://books.google.se/books?id=QUQxBwAAQBAJ.

[5] P. Childs, *Rotating Flow.* Butterworth-Heinemann, 2010. ISBN = 9780123820990, https://books.google.se/books?id=kMA49RH7cT0C.

[6] C. M. Sangan, O. J. Pountney, K. Zhou, M. Wilson, J. Michael Owen, and G. D. Lock, "Experimental measurements of ingestion through turbine rim seals—part i: Externally induced ingress," *Journal of Turbomachinery*, vol. 135, p. 021012, 11 2012. https://doi.org/10.1115/1.4006609.

[7] A. Bru Revert, P. F. Beard, and J. W. Chew, "Flow and ingestion in a turbine disc cavity under rotationally-dominated conditions," *International Journal of Turbomachinery, Propulsion and Power*, vol. 6, no. 3, 2021. https://doi.org/10.3390/ijtpp6030029.

[8] C. Cao, J. W. Chew, P. R. Millington, and S. I. Hogg, "Interaction of rim seal and annulus flows in an axial flow turbine," *Journal of Engineering for Gas Turbines and Power*, vol. 126, pp. 786–793, 11 2004. https://doi.org/10.1115/1.1772408.

[9] J. T. M. Horwood, F. P. Hualca, J. A. Scobie, M. Wilson, C. M. Sangan, and G. D. Lock, "Experimental and computational investigation of flow instabilities in turbine rim seals," *Journal of Engineering for Gas Turbines and Power*, vol. 141, p. 011028, 10 2018. https://doi.org/10.1115/1.4041115.

[10] L. Xie, Q. Du, G. Liu, Z. Lian, and J. Liu, "Flow characteristics in turbine wheel space cavity," *Energy Reports*, vol. 7, pp. 2262–2275, 2021. https://doi.org/10.1016/j.egyr.2021.04.014.

[11] A. M. Lapioli, *Experimental study on the effect of density ratio on the rotor-stator disc cavity purge flow.* PhD thesis, Politecnico di Torino, 2024. http://webthesis.biblio.polito.it/id/eprint/34278.

[12] D. Graikos, *Experimental Modelling of Gas Turbine Rim Seals.* PhD thesis, University of Bath, 2023.

https://researchportal.bath.ac.uk/en/studentTheses/experimental-modelling-of-gas-turbine-rim-seals.

[13] S. R. Burden, *Evaluation and application of CFD for turbine rim sealing.* PhD thesis, University of Surrey, 2024. https://doi.org/10.15126/thesis.901309.

[14] L. Orsini, A. Picchi, B. Facchini, A. Bonini, and L. Innocenti, “Impact of the purge flow density ratio on the rim sealing effectiveness in hot gas ingestion measurements,” *Journal of Turbomachinery*, vol. 146, p. 021002, 10 2023. https://doi.org/10.1115/1.4063755.

[15] A. Shapiro, *The Dynamics and Thermodynamics of Compressible Fluid Flow, Volume 1.* Engineering special collection, Wiley, 1953. ISBN = 9780471066910, https://books.google.se/books?id=675gtgEACAAJ.

[16] J. W. Daily and R. E. Nece, “Chamber dimension effects on induced flow and frictional resistance of enclosed rotating disks,” *Journal of Basic Engineering*, vol. 82, pp. 217–230, 03 1960. https://doi.org/10.1115/1.3662532.

[17] J. M. Owen, “Prediction of ingestion through turbine rim seals—part ii: Externally induced and combined ingress,” *Journal of Turbomachinery*, vol. 133, p. 031006, 11 2010. https://doi.org/10.1115/1.4001178.

[18] J. M. Owen, “Prediction of ingestion through turbine rim seals—part i: Rotationally induced ingress,” *Journal of Turbomachinery*, vol. 133, p. 031005, 11 2010. https://doi.org/10.1115/1.4001177.

[19] J. A. Scobie, C. M. Sangan, J. Michael Owen, and G. D. Lock, “Review of ingress in gas turbines,” *Journal of Engineering for Gas Turbines and Power*, vol. 138, p. 120801, 07 2016. https://doi.org/10.1115/1.4033938.

[20] F. Gao, J. W. Chew, P. F. Beard, D. Amirante, and N. J. Hills, “Large-eddy simulation of unsteady turbine rim sealing flows,” *International Journal of Heat and Fluid Flow*, vol. 70, pp. 160–170, 2018. https://doi.org/10.1016/j.ijheatfluidflow.2018.02.002.

[21] L. Davidson *et al.*, “Fluid mechanics, turbulent flow and turbulence modeling,” *Chalmers University of Technology, Goteborg, Sweden (Nov 2011)*, vol. 71, 2018.

[22] C. Ansys, “Ansys cfx solver theory guide,” *Ansys CFX Release 2024 R2*, 2024.

[23] F. Menter, “Stress-Blended Eddy Simulation (SBES)—A New Paradigm in Hybrid RANS-LES Modeling", booktitle="Progress in Hybrid RANS-LES Modelling,” (Cham), pp. 27–37, Springer International Publishing, 2018. https://doi.org/10.1007/978-3-319-70031-1_3.

[24] F. R. Menter, “Best practice: scale-resolving simulations in ansys cfd,” *ANSYS Germany GmbH*, 2021.

[25] J. T. M. Horwood, F. P. Hualca, M. Wilson, J. A. Scobie, C. M. Sangan, G. D. Lock, J. Dahlqvist, and J. Fridh, “Flow instabilities in gas turbine chute seals,” *Journal of Engineering for Gas Turbines and Power*, 2020. https://doi.org/10.1115/1.4045148.

A

Appendix

A.1 SBES: Mesh evaluation

The scale resolving simulations, like that of SBES, has strict mesh requirements which affect the accuracy of the solutions. Since the initial mesh was designed with these requirements in mind, no additional refinement were made. However, prior to SBES simulation, Length Scale Ratio (LSR), is calculated to verify the mesh quality. The LSR is defined as in Equation A.1. The minimum requirement is >5 and a recommended value is >10 based on Ansys guidelines [24].

$$LSR = \frac{L_t}{\sqrt[3]{Cell\,Volume}} \tag{A.1}$$

The RANS results were used to evaluate the LSR and an isovolume representation of unsuitable cells are shown in Figure A.1. As evident from the figure, no volume exists within the cavity except for the regions at the walls, which is appropriate as this is the boundary layer where RANS model will be adopted.

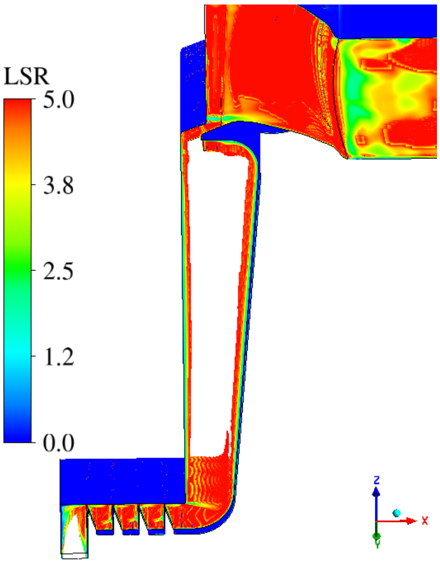

Figure A.1: Isovolume of cavity with a limiter of ≤ 5.

A.2 SBES: Shielding function

The shielding function helps identify regions where LES is used and where the RANS model is applied. For DR =1, $\Phi_o = 0.025$, this function is shown in the Figure A.2, with blue representing LES regions and red representing RANS regions.

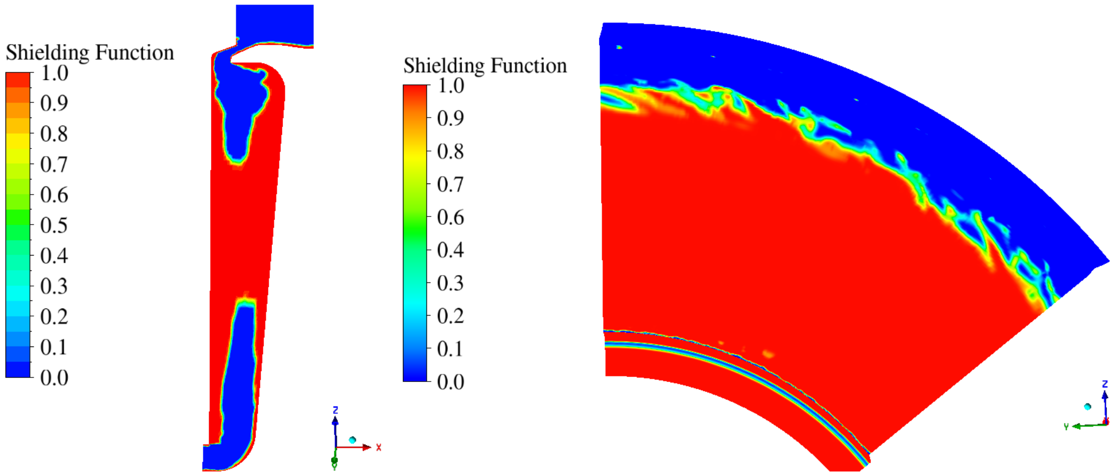

(a) Meridional View

(b) Tangential view

Figure A.2: Contour plot of shielding function at 7 revolutions.

DEPARTMENT OF MECHANICS AND MARITIME SCIENCES
CHALMERS UNIVERSITY OF TECHNOLOGY
Gothenburg, Sweden 2025
www.chalmers.se